Environmental Effects on Aerosol-Cloud Interaction in non-precipitating MBL Clouds over the Eastern North Atlantic

Xiaojian Zheng[1], Baike Xi[1], Xiquan Dong[1], Peng Wu[2], Timothy Logan[3] and Yuan Wang[4,5]

[1]Department of Hydrology and Atmospheric Sciences, University of Arizona, Tucson, AZ, USA

[2]Pacific Northwest National Laboratory, Richland, WA, USA

[3]Department of Atmospheric Sciences, Texas A&M University, College Station, TX, USA

[4]Division of Geological and Planetary Sciences, California Institute of Technology, Pasadena, CA, USA

[5]Jet Propulsion Laboratory, California Institute of Technology, Pasadena, CA, USA

Correspondence: Baike Xi (baikex@arizona.edu)

Abstract. Over the eastern north Atlantic (ENA) ocean, a total of 20 non-precipitating single-layer marine boundary layer (MBL) stratus and stratocumulus cloud cases are selected to investigate the impacts of the environmental variables on the aerosol-cloud interaction (ACI_r) using the ground-based measurements from the Department of Energy Atmospheric Radiation Measurement (ARM) facility at the ENA site during 2016 – 2018. The ACI_r represents the relative change of cloud-droplet effective radius r_e with respect to the relative change of cloud condensation nuclei (CCN) number concentration at 0.2% supersaturation ($N_{CCN,0.2\%}$) in the water vapor stratified environment. The ACI_r values vary from -0.01 to 0.22 with increasing sub-cloud boundary layer precipitable water vapor (PWV_{BL}) conditions, indicating that r_e is more sensitive to the CCN loading under sufficient water vapor supply, owing to the combined effect of enhanced condensational growth and coalescence processes associated with higher N_c and PWV_{BL}. The principal component analysis shows that the most pronounced pattern during the selected cases is the co-variations of the MBL conditions characterized by the vertical component of turbulence kinetic energy (TKE_w), decoupling index (D_i), and PWV_{BL}. The environmental effects on ACI_r emerge after the data are stratified into different TKE_w regimes. The ACI_r values, under both relatively lower and higher PWV_{BL} conditions, increase more than double from the low TKE_w to high TKE_w regime. It can be explained by the fact that stronger boundary layer turbulence maintains a well-mixed MBL, strengthening the connection between cloud microphysical properties and the below-cloud CCN and moisture sources. With sufficient water vapor and low CCN loading, the active coalescence

process broadens the cloud droplet size spectra, and consequently results in an enlargement of r_e. The enhanced activation of CCN and the cloud droplet condensational growth induced by the higher below-cloud CCN loading can effectively decrease r_e, which jointly presents as the increased ACI_r. This study examines the importance of environmental effects on the ACI_r assessments and provides observational constraints to future model evaluations on aerosol-cloud interactions.

1. Introduction

Clouds are one of the most important parts of the Earth's climate system. They can impact the global climate by modulating the radiative balance in the atmosphere. Moreover, the radiative effects of cloud adjustments due to aerosols remain one of the largest uncertainties in climate modeling (IPCC, 2013). Over the oceanic area, the lower troposphere is dominated by marine boundary layer (MBL) clouds. MBL clouds can persistently reflect the solar radiation by their long-lasting nature maintained by cloud-top radiative cooling, and therefore act as a major modulator of the Earth's radiative budget (Seinfeld et al., 2016). The climatic importance of MBL cloud radiative properties is primarily induced by cloud microphysical properties, such as cloud-droplet number concentration (N_C) and effective radius (r_e), and has been intensively investigated by many researchers (Garrett and Zhao, 2006; Rosenfeld, 2007; Wood et al., 2015; Seinfeld et al., 2016). The ambient aerosol conditions can influence these cloud microphysical properties via the aerosol-cloud interaction (ACI). Compared to the clean regions, clouds under the regions having relatively higher below-cloud aerosol concentrations exhibited smaller cloud droplets (reduced r_e and increased N_C) and enhanced both cloud liquid water contents and optical depths (McComiskey et al., 2009; Chen et al., 2014; Wang et al., 2018). The changes of MBL cloud microphysical properties induced by aerosols have been investigated from previous studies using in-situ measurements, ground- and satellite-based observations, and model simulations in multiple oceanic areas such as the eastern Pacific and eastern Atlantic (Twohy et al., 2005; Lu et al., 2007; Hill et al., 2009; Costantino and Bréon, 2010; Mann et al., 2014; Dong et al., 2015; Diamond et al., 2018; Yang et al., 2019; Zhao et al., 2019; Wang et al., 2020).

The assessments of ACI, particularly using ground-based remote sensing, vary in terms of the quantitative values, which represent the different cloud susceptibilities to aerosol loadings. Owing to the numerous approaches in assessing the ACI, such as the spatial and temporal scales, N_c and r_e retrieval methods, and more importantly, the different aerosol proxies used in the ACI quantification, different ACI results could be achieved. For example, the studies using total aerosol number concentration and

Deleted: N_c conversion

Deleted: more intrusions of

Deleted: Earth

Deleted: , namely the

Deleted:),

Deleted: more small

78 aerosol scattering/extinction coefficients to represent the aerosol loadings would result in relatively lower
79 ACI values (Pandithurai et al., 2009; Liu et al., 2016). This is primarily attributed to the inclusion of
80 aerosol species with different abilities to activate, which is determined by their physicochemical
81 properties, and thus will cause non-negligible uncertainties in capturing the information of aerosol
82 intrusion to the cloud (Feingold et al. 2006; Logan et al., 2014). While some studies found relatively
83 higher ACI values using cloud condensation nuclei (CCN) number concentration (N_{CCN}), presumably
84 due to the fact that CCN represents the portion of aerosols that can be activated and possesses the
85 potential ability to further grow into cloud droplets, this favorably yields a more straightforward
86 assessment of ACI (McComiskey et al., 2009; Qiu et al., 2017; Zheng et al., 2020). It is noteworthy that
87 the ACI variations have been found to have both increasing and decreasing trends in response to changing
88 environmental water availability (Martin et al., 2004; Kim et al., 2008; McComiskey et al., 2009;
89 Pandithurai et al., 2009; Martin et al., 2011; Liu et al., 2016; Zheng et al., 2020). Although these
90 contradicting results have been postulated due to multiple factors such as cloud adiabaticity,
91 condensational growth, collision coalescence, and atmospheric thermodynamics and dynamics, the
92 underlying mechanisms in altering the ACI and causing the uncertainties in the ACI assessments remain
93 unclear. Therefore, further studies are necessary (Fan et al., 2016; Feingold and McComiskey, 2016;
94 Seinfeld et al., 2016).

95   The Eastern North Atlantic (ENA) is a remote oceanic region that features persistent but diverse
96 subtropical MBL clouds, owing to complex meteorological influences from the semi-permanent Azores
97 High and prevailing large-scale subsidence (Wood et al., 2015). The ENA has become a favorable region
98 to study the aerosol indirect effects on MBL clouds under a relatively clean environment with occasional
99 intrusions of long-range transport of continental air mass (Logan et al., 2014; Wang et al., 2020). The
100 atmospheric radiation measurement (ARM) program established the ENA permanent observatory site on
101 the northern edge of Graciosa Island, Azores, in 2013, which continuously provides comprehensive
102 measurements of the atmosphere, radiation, cloud, and aerosol from ground-based observation
103 instruments. Owing to the location of the site, which sits in between the boundaries of mid-latitude and
104 subtropical regimes, the ENA is under the mixed influence of diverse meteorological conditions. In terms
105 of the aerosol influence on the cloud properties, the roles of meteorological factors on cloud formation
106 and development are not negligible and hence are being explored in this study. The large-scale
107 thermodynamic variables of the lower troposphere are widely used, such as the lower tropospheric
108 stability (LTS), where the higher LTS values are found to be associated with a relatively shallow and
109 well-mixed marine boundary layer, and are prone to stratiform cloud formations with higher cloud
110 fractions (Klein and Hartmann, 1993; Wood, 2012; Wood and Bretherton, 2006; Yue et al., 2011;

Deleted: where

Deleted: So that in

Rosenfeld et al., 2019), especially over the subtropical ocean such as the northeast Atlantic. Over the ENA site, the spatial gradient of the LTS has been studied to be associated with the contribution terms of MBL turbulence and the wind directional change (Wu et al., 2017).

In the cloud-topped MBL which is maintained by cloud-top radiative cooling, the buoyancy generation and shear contribute most to the turbulence kinetic energy (TKE) production (Nicholls, 1984; Hogan et al., 2009), where the intensity of turbulence denotes the coupling of MBL clouds to the below-cloud boundary layer. In terms of the cloud droplet growth process, especially in a clean environment with low N_{CCN} below the cloud layer, the cloud droplets at the cloud base experience rapid growth via the diffusion of water vapor, and subsequently enter the regime of active coalescence (Rosenfeld and Woodley, 2003; Martins et al., 2011). The intensive turbulence effectively modulates the cloud droplet growth by strengthening the coalescence process and the cloud cycling (Feingold et al., 1996, 1999; Pawlowska et al., 2006). In particular, the unique topography of Graciosa Island induces an island effect which could cause disturbances in the updraft and hence impact the MBL turbulence, depending on the surface wind directions (Zheng et al., 2016). The environmental effects on the MBL cloud formation and development processes and cloud microphysical properties have been widely implemented and considered in climate modeling (Medeiros and Stevens, 2011; West et al., 2014; Zhang et al., 2016). Thus, it is important to provide observational constraints on the environmental effects. The assessment of ACI from the ground-based perspective highly relies on the sensitivities of cloud droplet number concentrations and size distribution to the changing of below-cloud CCN loadings. Hence, studying the relationship between the environmental effect and the MBL cloud microphysical responses is a nontrivial task.

In this study, we target the non-precipitating single-layer MBL stratus and stratocumulus clouds during the period between September 2016 and May 2018 and examine the role of thermodynamical and dynamical variables on ACIs. This study aims to advance the understanding of ACI by disentangling the environmental effects and providing observational constraints on quantifying the ACI when modeling aerosol effects on MBL clouds. The ground-based observations and retrievals, and the reanalysis are introduced in section 2. Section 3 describes the aerosol, cloud and meteorological properties, and the variations of cloud microphysical properties under different environmental regimes. Moreover, the ACIs under given water vapor conditions and the roles of environmental effects on ACI are discussed in Section 3. The conclusion of the key findings and the future work are presented in section 4.

2. Data and methods

2.1 Cloud and aerosol properties

155   The cloud boundaries at the ARM ENA site are primarily determined by the ARM Active Remotely-
156   Sensed Cloud Locations (ARSCL) product, which is a combination of data detected by multiple active
157   remote-sensing instruments, including the Ka-band ARM Zenith Radar (KAZR) and laser ceilometer.
158   The KAZR has an operating frequency at 35 GHz and is sensitive in cloud detection with very minimum
159   attenuation up to the cloud top height (Widener et al., 2012). The temporal and vertical resolutions of
160   KAZR reflectivity are 4 seconds and 30 m, respectively. The ceilometer operates at 910 nm and its
161   attenuated backscatter data can be converted to the cloud base height up to 7.7 km with an uncertainty
162   of ~10 m (Morris, 2016). Combing both KAZR and ceilometer measurements, the cloud base (z_b) and
163   top (z_t) heights can be identified accordingly. The single-layer low cloud is defined as having a cloud
164   top height lower than 3 km, with no additional cloud layer in the atmosphere above (Xi et al., 2010).

165   The cloud microphysical properties are retrieved from a combination of ground-based observations,
166   including KAZR, ceilometer, and microwave radiometer. The detailed retrieval methods and procedures
167   are described in Wu et al. (2020a). The retrieved cloud microphysical properties, both in time series and
168   vertical profiles, have been validated using the collocated aircraft in-situ measurements during the
169   Aerosol and Cloud Experiments in the Eastern North Atlantic field campaign (ACE-ENA). The retrieval
170   uncertainties are estimated to be ~15% for cloud droplet effective radius (r_e), ~35% for cloud droplet
171   number concentration (N_c), and ~30% for the cloud liquid water content (LWC) (Wu et al., 2020a).
172   Furthermore, the cloud adiabaticity is calculated using the retrieved in-cloud vertical profile of LWC and
173   the adiabatic LWC_{ad}. The LWC_{ad} is given by $\text{LWC}_{ad(z)} = \Gamma_{ad}(z - z_b)$, following the method in Wu et
174   al. (2020b), where Γ_{ad} denotes the linear increase of LWC with height under an ideal adiabatic condition
175   (Wood, 2005). The cloud adiabaticity (f_{ad}) is defined as the ratio of LWC to LWC_{ad}.

176   The surface CCN number concentrations (N_{CCN}) are measured by the CCN-100 (single-column)
177   counter. Since the supersaturation (SS) levels cycle between approximately 0.10% and 1.10%, within
178   one hour, N_{CCN} under a relatively stable supersaturation level has to be carefully calculated to rule out
179   the impact of supersaturation on N_{CCN}. This study adopts the interpolation method given by $N_{CCN} = cSS^k$
180   (Twomey, 1959), where parameters c and k are fitted by a power-law function for every periodic cycle.
181   In this study, the supersaturation level of 0.2% is used because it represents typical supersaturation
182   conditions of boundary-layer stratiform clouds (Hudson and Noble, 2013; Logan et al., 2014; Wood et
183   al., 2015; Siebert et al., 2021), and N_{CCN} at 0.2% supersaturation (hereafter $N_{CCN,0.2\%}$) is interpolated to
184   a 5-min temporal resolution.
185

186   **2.2 Environmental conditions and cloud case selections**

| Deleted: are set to cycling |
| Deleted: approximately |

189   The integrated precipitable water vapor (PWV) is obtained from a 3-channel microwave radiometer

190   (MWR3C), which operates at three frequency channels of 23.834, 30, and 89 GHz. The uncertainty of

191   PWV is estimated to be ~0.03 cm (Cadeddu et al., 2013). To capture the information of MBL water vapor

192   more accurately, the sub-cloud boundary layer integrated precipitable water vapor (PWV$_{BL}$) is calculated

193   using the interpolated sounding product following:

194    $\text{PWV}_{BL} = \frac{1}{\rho_w} \sum (z_{i+1} - z_i) * (\rho_{v,i+1} + \rho_{v,i})/2,$ (1)

195   where the ρ_w is the liquid water density and the ρ_v is the water vapor density collected from the

196   Interpolated Sounding and Gridded Sounding Value-Added Products (Toto and Jensen, 2016), the

197   subscripts i and $i + 1$ represent the bottom and top of each interpolated sounding height layer. Both

198   PWV and PWV$_{BL}$ are temporally collocated to 5-min resolutions and plotted against each other in Fig.

199   S1a to test the contribution of PWV$_{BL}$ to PWV. The Pearson correlation coefficient of 0.85 shows that

200   the PWV$_{BL}$ are strongly positively correlated with PWV, while the distribution of the percentage ratio of

201   PWV$_{BL}$ to PWV (Fig. S1b) indicates that, on average, PWV$_{BL}$ contributes to ~58% of PWV. Considering

202   the cloud-topped MBL, the majority of cases (~74%) associate with a relatively moist boundary layer

203   compared to the amount of water vapor in the free troposphere, where PWV$_{BL}$ already contributed over

204   50% of the total column PWV. In contrast, only ~9% of cloud samples occur under a relatively dry

205   boundary layer and moist free troposphere, where PWV$_{BL}$ contributions are less than 40%. In general,

206   PWV can well capture the variation of PWV$_{BL}$. In the rest of the study, PWV$_{BL}$ are used, as it represents

207   the sub-cloud boundary layer water vapor availability which is more closely related to the MBL cloud

208   processes.

209   The LTS parameter is used as a proxy of large-scale thermodynamic structure and is defined as the

210   difference between the potential temperature at 700 hPa and surface ($\theta_{700} - \theta_{sfc}$). The LTS values are

211   calculated from European Centre for Medium-Range Weather Forecasts (ECMWF) model outputs of

212   potential temperature, by averaging over a grid box of 0.56°×0.56° centered at the ENA site. To match

213   the temporal resolutions of the other variables, the original 1-hour LTS data are downscaled to 5-min

214   under the assumption that the large-scale forcing would not have significant changes within an hour.

215   The boundary layer decoupling condition is represented by the decoupling index (D_i), which is

216   given by $D_i = (z_b - z_{LCL})/z_b$, where the z_{LCL} is the lifting condensation level calculated analytically

217   following the method in Romps (2017), with an uncertainty of around 5 m. The surface temperature,

218   pressure, relative humidity, and mass fraction of water vapor are used in the z_{LCL} calculation, as long as

Deleted: resolution

Deleted: the

Deleted: the

Deleted: the

Deleted: contribute

Deleted: the

Deleted: the

Deleted: the

Deleted: the

Deleted: the

Deleted: availabilities

Deleted: are

Deleted: Romp

Deleted: that

the vector-averaged wind directions (in 360° coordinate) over the ENA site are obtained from the ARM

surface meteorology systems (ARM MET handbook, 2011).

As for the boundary layer dynamics, the higher-order moments of vertical velocity are widely used

in different model parameterization practices, such as higher-order turbulence closure and probability

density function methods (Lappen and Randall, 2001; Zhu and Zuidema, 2009; Ghate et al., 2010). The

vertical velocity variance can be used to represent the turbulence intensity in the below-cloud boundary

layer (Feingold et al., 1999). In this study, the vertical component of the turbulence kinetic energy (TKE_w)

is used, which is defined as:

$$TKE_w = \frac{1}{2} \overline{(w')^2} ,\qquad (2)$$

where the $(w')^2$ is the variance of vertical velocity measured from the Doppler lidar standard 10-min

integration, which is collected in the Doppler Lidar Vertical Velocity Statistics Value-Added Product

(Newson et al., 2019). The noise correction has been applied to reduce the uncertainty of the variance to

~10% (Hogan et al., 2009; Pearson et al., 2009). In this study, the mean value of TKE_w in the sub-cloud

boundary layer proportion of the Doppler lidar range is used, and the data temporal resolution is further

downscaled to 5-min for temporal collocation purposes.

In this study, the non-precipitating cloud periods are determined when the KAZR reflectivity at the

ceilometer-detected cloud base height range does not exceed -37 dBZ (Wu et al., 2015, 2020b), which

extensively rules out the wet-scavenging depletion on below-cloud CCN (Wood, 2006) and ensures the

accuracy in capturing the below-cloud CCN loadings. Both retrieved cloud microphysical properties and

CCN data are available from September 2016 to May 2018 and confine this period in this study.

3. Result and Discussion

3.1 Aerosol, cloud, and meteorological properties of selected cloud cases

A total of 20 non-precipitating cloud cases are selected in this study, with the detailed time periods

listed in Table 1, including 1143 samples with temporal resolutions of 5-min, which corresponds to ~95

hours. Among the selected cases, there are three, eight, five, and four cases for Spring, Summer, Fall,

and Winter seasons, respectively. MBL clouds often produce precipitation in the form of drizzle (Wood

2012, Wu et al., 2015, 2020b). A recent study of the seasonal variation of the drizzling frequencies (Wu

et al., 2020b) showed that the MBL clouds in the cold months (Oct-Mar) have the highest drizzling

frequency of the year (~70%), while the clouds in the warm months (Apr-Sept) are found to have a lower

chance of drizzling (~45%). Therefore, the selection of a non-precipitating single-layer low cloud case

266 that lasts at least 2 hours is limited, with only 6 cases found in the cold months and 14 cases found during
267 the warm months.

268 The probability distribution functions (PDFs) of the aerosol and cloud properties, and the
269 environmental conditions for the selected cases are shown in Fig. 1. The PDF of $N_{CCN,0.2\%}$ presents a
270 normal distribution with a mean value of 215 cm^{-3} and median value of 217 cm^{-3}. About 97% of the
271 $N_{CCN,0.2\%}$ samples lie below 350 cm^{-3} and represents a relatively clean environment (Logan et al., 2014,
272 2018). A few instances of aerosol intrusions (~3%) with higher $N_{CCN,0.2\%}$ were likely a result of
273 continental air mass transport from North America, Europe, and Africa (Logan et al., 2014; Wang et al.,
274 2020). As for the cloud microphysical properties, the cloud-layer mean N_c and r_e (Fig. 1b and 1c) are
275 also both normally distributed with median values close to the mean values. The majority of the N_c
276 values (~91%) are lower than 125 cm^{-3} with a mean value of 86 cm^{-3}, and the r_e distribution peaks
277 between 9 - 11 μm with a mean value of 10.1 μm. Both N_c and r_e values fall in the typical ranges of the
278 non-precipitating MBL cloud characteristics over the ENA site (Dong et al., 2014; Wu et al., 2020b).
279 The distribution of f_{ad} is slightly skewed to the left with a median value of 0.66 (Fig. 1d), indicating that
280 the bulk of cloud samples are close to adiabatic environments, while the left tail denotes a wide range of
281 cloud sub-adiabaticities, which allows us to investigate the role of cloud adiabaticities on the cloud
282 microphysical variations.

283 For all selected cases, the LTS, which represents the large-scale thermodynamic structure, is
284 distributed bimodally across the range from 14K to 23K with mean and median values of 19.1K in Fig.
285 1e. A higher LTS magnitude represents a relatively stable environment and is favorable to the formation
286 of marine stratocumulus (Medeiros and Stevens, 2011; Gryspeerdt et al., 2016). Note that the median
287 LTS of 19.1 K in this study is close to the separation threshold of 18.55K suggested by prior studies to
288 distinguish the marine stratocumulus from a global assessment of marine shallow cumulus clouds
289 (Smalley and Rapp, 2020). Therefore, leveraging the demarcation line at 19.1K may allow us to
290 investigate the aerosol-cloud relationships under contrasting thermodynamic regimes. The PDF of D_i
291 parameter spreads widely with a median value of 0.34 for the selected cases (Fig. 1f), which provides an
292 opportunity to study the cloud sample behaviors under MBL conditions range from well-mixed to
293 decoupled. Higher D_i values indicate more decoupled MBL with weaker turbulence which cannot
294 sufficiently maintain the well-mixed MBL, while lower D_i values often associate with stronger
295 turbulence which maintains a coupled MBL (Jones et al., 2011). As an indicator of the below-cloud
296 boundary layer turbulence, the TKE_w values present a gamma distribution that is highly skewed to the
297 right (Fig. 1e), with a mean value of 0.11 and a median value of 0.08 m^{2}s^{-2}. About half of the cloud

300 samples are observed within a relatively less turbulent environment (which is also implied by the higher

301 half of D_i), suggesting weak connections between the cloud layer and the below-cloud boundary layer.

302 The other half of the cloud samples, with relatively higher TKE_w values up to 0.4 m^2/s^2, imply tighter

303 connections between cloud microphysical properties and below-cloud boundary layer accompanied by

304 intensive turbulent conditions, which is favorable to enhance cloud droplet growth (Albrecht et al., 1995;

305 Hogan et al., 2009; Ghate et al., 2010; West et al., 2014; Ghate and Cadeddu, 2019).

306   It is noteworthy that PWV_{BL} values exhibit a bimodal distribution with a median value of 1.2 cm

307 (Fig. 1f). About 49% of the samples have their PWV_{BL} values in the range of 0.4 - 1.2 cm with the first

308 peak in 0.6 - 0.8 cm, and 51% of the samples have PWV_{BL} values higher than 1.2 cm with a second peak

309 in 1.6 - 1.8 cm, which may be due to the seasonal difference of the selected cases. Fig. S2 shows the

310 seasonal variation of the PWV_{BL} from 2016 to 2018 when single-layered low clouds are present. The

311 monthly PWV_{BL} values are as low as ~ 0.9 cm and remain nearly invariant from January through March,

312 then increase to ~ 2.0 cm (doubled) in September, and decrease dramatically to the winter months. The

313 selected cloud cases are distributed across the seasons, with ~34% of the samples occurring during the

314 months with the lowest mean PWV_{BL} (Jan-Mar), while ~43% of the samples fall in the highest PWV_{BL}

315 months (Jun-Sept). These two different PWV_{BL} regions will provide a great opportunity for us to further

316 examine the ACI under relatively lower and higher water vapor conditions.

317

318 **3.2 Dependent of cloud microphysical properties on CCN and PWV_{BL}**

319   Figure 2 shows the cloud microphysical properties as a function of $N_{CCN,0.2\%}$ and PWV_{BL} for the

320 samples from 20 selected cases. As illustrated in Fig. 2a, there is a statistically significant positive

321 correlation (R^2=0.9) between $ln(N_c)$ and $\ln(N_{CCN,0.2\%})$. The linear fit of $ln(N_c)$ to $\ln(N_{CCN,0.2\%})$ is then

322 mathematically transformed to a power-law fitting function of N_c to $N_{CCN,0.2\%}$, and plotted as dash lines

323 in Fig. 2a. The power-law fitting indicates that 90.3% of the variation in binned $ln(N_c)$ can be explained

324 by the change in the binned $ln(N_{CCN,0.2\%})$ and further suggests that with more available below-cloud

325 CCN, higher number concentrations are expected. The logarithmic ratio $\partial ln(N_c)/\partial ln(N_{CCN,0.2\%})$ is

326 computed to be 0.435 from our study. This ratio is very close to 0.48 as was shown by McComiskey et

327 al. (2009), who also used ground-based measurements to study the marine stratus clouds over the

328 California coast. The logarithmic ratio (0.435) is also close to the result (0.458) of Lu et al. (2007) who

329 used aircraft in-situ measured cloud droplet and accumulation mode aerosol number concentration for

330 the marine stratus and stratocumulus clouds over the eastern Pacific Ocean. The ratio reflects the relative

331 conversion efficiency of cloud droplets from the CCN, regardless of the water vapor availability.

335   Theoretically, it has the boundaries of 0 - 1, where the lower bound means no change of N_c with N_{CCN},
336   and the upper bound indicates a linear relationship that every CCN would result in one cloud droplet.
337   Our result is comparable with the previous studies targeting the MBL stratiform clouds, indicating a
338   certain similarity of the bulk cloud microphysical responses with respect to aerosol intrusion in those
339   types of cloud and over different marine environments, further support that the assessment in this study
340   is valid.

341   The PWV_{BL} values are represented as blue circles (larger one for higher PWV_{BL}) in Fig. 2a in order
342   to study the role of water vapor availability on the CCN-N_c conversion process. As demonstrated in Fig.
343   2a, the PWV_{BL} values almost mimic the increasing $N_{CCN,0.2\%}$ trend, which is also governed by the
344   seasonal $N_{CCN,0.2\%}$ and the selected cloud cases. Fig. S3 shows the seasonal variation of $N_{CCN,0.2\%}$ from
345   2016 to 2018. It is noticeable that the monthly $N_{CCN,0.2\%}$ values, which mimic the monthly variation of
346   PWV_{BL}, are much higher during warm months (May-Oct) than during cold months (Nov-Apr). This
347   seasonal $N_{CCN,0.2\%}$ variation is also found in recent studies of MBL aerosol composition and number
348   concentration. During the warm months, the below-cloud boundary layer is enriched by the accumulation
349   mode of sulfate and organic particles via local generation and long-range transport induced by the semi-
350   permanent Azores High, which are found to be hydrophilic and can be great CCN contributors (Wang et
351   al., 2020; Zawadowicz et al., 2020; Zheng et al., 2018, 2020). Therefore, the coincidence of high
352   $N_{CCN,0.2\%}$ and PWV_{BL} does not necessarily imply a physical relationship, but instead is the result of their
353   similar seasonal trend. The potential co-variabilities between $N_{CCN,0.2\%}$ and PWV_{BL}, and hence the
354   implication on the N_c variation will be further investigated in the latter section. When taking the PWV_{BL}
355   into account, R^2 increases from 0.903 to 0.982, and this new relationship suggests that the co-variability
356   between the binned $ln(N_{CCN,0.2\%})$ and ln (PWV_{BL}) are in a stronger correlation with the change in
357   binned $ln(N_c)$. Intuitively, if the CCN-N_c relationship is primarily dominated by the diffusion of water
358   vapor, more CCN and higher PWV_{BL} should result in a continuously increasing of N_c. However, the
359   rapid increase of N_c (37 to 92 cm^{-3}) in the first half of $N_{CCN,0.2\%}$ bins (<250 cm^{-3}) does not happen in
360   the second half of the $N_{CCN,0.2\%}$ bins (>250 cm^{-3}) where the slope of N_c increase (96 to 103 cm^{-3})
361   appears to be flattened for higher $N_{CCN,0.2\%}$ and PWV_{BL} bins. Furthermore, the joint power-law fitting of
362   N_c (to $N_{CCN,0.2\%}$ and PWV_{BL}) appears to be constantly lower than the single power-law fitting of N_c (to
363   $N_{CCN,0.2\%}$ solely) in each bin. The negative power of PWV_{BL} in this relationship suggests that PWV_{BL}
364   might play a stabilization role in the diffusional growth process, which will be further analyzed in the
365   following sections.

366   The relationship between r_e and $N_{CCN,0.2\%}$ is shown in Fig. 2b where there is no significant

367   relationship between r_e with $N_{CCN,0.2\%}$ solely, given a near-zero slope and the low correlation coefficient

368   (fitted line not plotted). However, after applying a multiple linear regression to the logarithmic form of

369   r_e, $N_{CCN,0.2\%}$ and PWV$_{BL}$, a significant correlation among those three variables is found. The r_e is

370   negatively correlated with $N_{CCN,0.2\%}$ and positively correlated with PWV$_{BL}$, and 73.7% of the variations

371   in binned $ln\,(r_e)$ can be explained by the joint changes of the binned $ln(N_{CCN,0.2\%})$ and $ln\,(\text{PWV}_{BL})$.

372   This indicates that in the bulk part, r_e decreases with increasing $N_{CCN,0.2\%}$ and enlarges with increasing

373   PWV$_{BL}$. Notice that in the lower $N_{CCN,0.2\%}$ bins (<150 cm^{-3}) where the PWV$_{BL}$ values are the lowest

374   among all the bins (0.76 – 0.85 cm), the limitation of cloud droplet growth by competing for the available

375   water vapor is evident by the changes in N_c and r_e. For example, the $N_{CCN,0.2\%}$ changes from 47 to 128

376   cm^{-3}, the N_c increases from 37 to 71 cm^{-3} and r_e only increases from 9.30 to 9.74 µm. In other words,

377   nearly tripling the CCN loading leads to roughly doubling N_c, while the r_e is only enlarged by 0.44 µm

378   (4.7%). In the relatively low available PWV$_{BL}$ regime, it is clear that even with more CCN being

379   converted into cloud droplets, the limited water vapor condition prohibits the further diffusional growth

380   of those cloud droplets. However, in the higher $N_{CCN,0.2\%}$ bins (>150 cm^{-3}) with relatively higher

381   PWV$_{BL}$, the binned r_e values fluctuate and decrease with increasing CCN bins under similar PWV$_{BL}$ (i.e.,

382   the two $N_{CCN,0.2\%}$ ranges from 200-400 cm^{-3}, and from 400-500 cm^{-3}). Since r_e essentially represents

383   the area-weighted information of the cloud droplet size distribution (DSD), this sorting method of r_e

384   inevitably entangles multiple cloud droplet evolution processes and environmental effects that can alter

385   the DSD, especially under the condition of sufficient water supply. Therefore, the further assessment of

386   the r_e responses to the $N_{CCN,0.2\%}$ loading under the constraint of water vapor should be discussed in order

387   to untangle the impacts of different processes and environmental effects on r_e.

388

389   **3.3 Aerosol-cloud interaction under different water vapor availabilities**

390   As previously discussed above and suggested by earlier studies, the conditions of water vapor

391   supply have a substantial impact on various processes from CCN-N_c conversion to in-cloud droplet

392   condensational growth and coalescence processes, hence effectively altering the cloud DSD (Feingold et

393   al., 2006; McComiskey et al., 2009; Zheng et al., 2020). Moving forward to examine how r_e responds to

394   the changes of $N_{CCN,0.2\%}$ in the context of given water vapor availability, an index describing the aerosol-

395   cloud interaction process is introduced as follows:

396    $\text{ACI}_r = -\dfrac{\partial \ln\,(r_e)}{\partial \ln\,(N_{CCN,0.2\%})}\bigg|_{\text{PWV}_{BL}}.$ \hfill (3)

397   The ACI_r represents the relative change of r_e with respect to the relative change of $N_{CCN,0.2\%}$, where

398   positive ACI_r denotes the decrease of r_e with increasing $N_{CCN,0.2\%}$ under binned PWV_{BL}. This

399   assessment of ACI_r focuses on the relative sensitivity of the cloud microphysics response in the water

400   vapor stratified environment, while previous studies used the cloud liquid water path (LWP) as the

401   constraint (Twomey, 1977; Feingold et al., 2003; Garrett et al., 2004). LWP describes the liquid water

402   (i.e., existing cloud droplets) physically linked to r_e and N_c which have an interdependent relationship

403   in cloud retrieval procedures, and hence to a certain extent, share co-variabilities with cloud

404   microphysical properties (Dong et al., 1998; Wu et al., 2020a). In this study, by using the PWV as a

405   sorting variable, we are trying to capture the role of ambient available water vapor in the cloud droplet

406   growth process (especially the water vapor diffusional growth), using measurement independent to the

407   cloud retrievals. Fig. 3 shows the variation of ACI_r under different PWV_{BL} bins, and illustrates the

408   calculation of ACI_r in three different PWV_{BL} ranges. Note that in Fig. 3a, the regressions are derived

409   from all points (statistically significant with a confidence level of 95%). As shown in Fig. 3a, the ACI_r

410   values range from close-to-zero values (-0.01) to 0.22, with the mean value of 0.117 ± 0.052. The ACI_r

411   range of this study agrees well with the previous studies of MBL cloud aerosol-cloud interactions

412   (McComiskey et al., 2009; Pandithurai et al., 2009; Liu et al., 2016). It is noteworthy that the variation

413   of ACI_r with PWV_{BL} suggests two different relationships under separated PWV_{BL} conditions, as

414   discussed in the following two paragraphs.

415   Under the relatively lower PWV_{BL} condition (<1.2 cm), the low values of ACI_r (-0.01 - 0.057)

416   indicate that r_e is less sensitive to $N_{CCN,0.2\%}$, and the dependence on PWV_{BL} is also insignificant as given

417   by flat regression line (green dashed line) and low correlation coefficient of 0.38 (Fig. 3a). As discussed

418   in section 3.2, the limited water vapor can weaken the ability of condensational growth of the cloud

419   droplet converted from CCN, that is, the increase of CCN loading cannot be effectively reflected by a

420   decrease in r_e. For example, a 307% increase of $N_{CCN,0.2\%}$ only leads to a 10% decrease in r_e in the

421   PWV_{BL} range of 0.8-1.0 cm as shown in Fig. 3b. So that in this regime, even with a slight PWV_{BL} increase,

422   the lack of a sufficient amount of large cloud droplets is favorable to the predominant condensational

423   growth process, which effectively narrows the cloud DSD and, in turn, confines the variable range of r_e

424   with respect to $N_{CCN,0.2\%}$ (Pawlowska et al., 2006; Zheng et al., 2020). In this situation, the ability of

425   CCN to convert to cloud droplets as well as droplet condensational growth are limited by insufficient

426   water vapor, rather than an influx of CCN.

427   However, under the relatively higher PWV_{BL} regime (>1.2 cm), the ACI_r values become more

428   positive and express a significant increasing trend with PWV_{BL} (correlation coefficient of 0.83, blue

432   dashed line), which indicates that r_e is more susceptible to $N_{CCN,0.2\%}$ in this regime. On the one hand,

433   due to the sufficient water vapor supply, the enhanced condensational growth process allows more CCN

434   to grow into cloud droplets, so that the limiting factor of the droplet growth corresponds to the changes

435   in CCN loading. On the other hand, the increased N_c values associated with higher water vapor supply

436   in the cloud effectively enhance the coalescence process. This results in broadening the cloud DSD and

437   increasing the variation range of r_e in response to the changes of $N_{CCN,0.2\%}$. To test our hypothesis of

438   active coalescence under higher water vapor conditions, Table 2 lists the occurrence frequencies of large

439   r_e values (> 12 and 14 µm) under the six high PWV$_{BL}$ bins (1.2 – 2.4 cm), because this range of 12-14

440   µm can serve as the critical demarcation of an efficient coalescence process (Gerber, 1996; Freud and

441   Rosenfeld, 2012; Rosenfeld et al., 2012). As listed in Table 2, for the six high PWV$_{BL}$ bins, the

442   occurrence frequencies of r_e>12 µm are 25.0%, 30.6%, 54.1%, 74.2%, 93.8%, and 97.5%, and the

443   occurrence frequencies of r_e>14 µm are 1.25%, 1.77%, 7.4%, 17.7%, 31.9%, and 20.1%, respectively.

444   The increasing trends of large r_e occurrences mimic the trend of ACI$_r$ and suggest that with

445   increased PWV$_{BL}$, cloud droplets have a greater chance to grow via the effective coalescence process

446   and subsequently lead to an enlargement of ACI$_r$. Although previous studies have brought up the

447   potential impacts of the cloud droplet coalescence process on ACI, it is rarely seen that the relationship

448   among them has been discussed in detail. Here we provide possible explanations on how the enhanced

449   coalescence process can enlarge ACI$_r$. Quantitatively, ACI$_r$ is described by the logarithmic partial

450   derivative ratio of r_e to $N_{CCN,0.2\%}$, thus a sharper decrease of r_e with respect to a given $N_{CCN,0.2\%}$ range

451   can result in a steeper slope and in turn, larger ACI$_r$ (i.e., a 239% increase in $N_{CCN,0.2\%}$ leads to a r_e

452   decrease of 48% in the 2.2-2.4 cm bin in Fig. 3b). Physically, this relies on how the cloud droplet size

453   distribution (DSD) would change with different CCN loadings. Therefore, particularly in low CCN

454   conditions, sufficient water vapor availability will allow cloud droplets to continuously grow via

455   diffusion of water vapor (i.e., condensational growth), and enter the active cloud-droplet coalescence

456   regime. In contrast, the increase in cloud droplet size can effectively reduce N_c via the process of large

457   cloud droplets collecting small droplets, and small droplets be coalesced into large droplets.

458   Consequently, the cloud DSD becomes effectively broadened toward the large tail by the coalescence,

459   so that r_e is enlarged. With more CCN available, the cloud DSD is narrowed by the enhanced

460   condensational growth and regresses toward the small tail by increasing the amount of newly converted

461   cloud droplets which result in decreased r_e. These interactions between CCNs and cloud droplets

462   ultimately result in the broadened changeable range of r_e, and in turn, the enlarged ACI$_r$.

466   In order to investigate the theoretical implication of supersaturation conditions on the aerosol-cloud
467   interaction observed here in the MBL stratiform clouds, the ACI_r values are calculated with respect to
468   the surface N_{CCN} theoretically at two additional high supersaturation levels (0.5% and 1.2%), under all
469   PWV_{BL} conditions. The results in Table 3 show that the ACI_r signals are both weak and do not have
470   significant changes under relatively lower PWV_{BL} conditions, while the ACI_r signals tend to strengthen
471   with the increase of supersaturation under the relatively higher PWV_{BL}. Based on Köhler theory, if the
472   supersaturation exceeds the critical point for the given droplet, the droplet will thus experience continued
473   growth, so theoretically the ACI should increase with the supersaturation under same aerosol number
474   concentration. However, the observed limited water vapor cannot support this ideal droplet growth,
475   results in weak responses of cloud droplets to aerosol intrusion. With the increase of observed water
476   vapor, the continued growth of cloud droplets becomes more plausible, hence the high supersaturation
477   yields larger droplets with low number of aerosols, more efficient droplet activation with a large number
478   of aerosols, and in turns, larger ACI_r (even out of the theoretical bounds). However, considering these
479   high supersaturation environments are unphysical in the observed MBL cloud layers, and estimating the
480   real supersaturation conditions using ground-based remote-sensing is beyond the scope of this study, we
481   chose the supersaturation level of 0.2% because it represents the most typical supersaturation conditions
482   of MBL stratiform clouds.
483
484   **3.4 The co-variabilities of the meteorological factors**
485   The environmental conditions over the ENA have been widely studied as not independent but
486   entangled with each other (Wood et al., 2015; Zheng et al., 2016; Wu et al., 2017; Wang et al., 2021).
487   To better understand the dependencies and the co-variabilities of the meteorological factors, a principal
488   component analysis (PCA) is performed comprising the following variables: (1) PWV_{BL} denotes the
489   water vapor availability within the boundary layer; (2) D_i describes the boundary layer coupling
490   conditions; (3) TKE_w represents the strength of boundary layer turbulence; (4) $W_{dir,NS}$ reflects the
491   surface wind directions in terms of northerly and southerly; and (5) LTS infers the large-scale
492   thermodynamic structures. Note that the $W_{dir,NS}$ are taken as $W_{dir,NS} = abs(W_{dir} - 180°)$, so that the
493   original W_{dir} (0-360°) can be transformed to $W_{dir,NS}$ (0-180°) where the values smaller than 90° are
494   close to the southerly wind, and those greater than 90° are close to the northerly wind. The $W_{dir,ns}$ are
495   transformed as such to capture the island effects better, because the cliff is located north of the ENA site.
496   The input data metric of the PCA is constructed from the above five variables, thus the principal
497   components (PCs) that explaining the variations of those dependent variables can be output from the

505 eigenanalysis. The result shows that for the five selected meteorological factors, the proportions of the

506 total intervariable variance explained by the PCs are 43.72%, 22.01%, 18.26%, 8.95% and 7.06%, and

507 the eigenvalues are 2.19, 1.10, 0.91, 0.45, and 0.35, respectively. Note that the first three PCs have the

508 highest eigenvalues and explain most (~84%) of the total variance, which indicates that they can capture

509 the significant variation patterns of the selective meteorological factors.

510 To determine the relative contributions of the variables to PCs, all the five selected meteorological

511 variables are projected to the first three PCs and the Pearson correlation coefficients between them are

512 listed in Table 4. For the first PC (PC1) which accounts for the highest proportion (43.72%) of the total

513 variance, the PC1 is strongly negatively correlated with PWV_{BL} (-0.84) and D_i (-0.73), but strongly

514 positively correlated with TKE_w (0.69). These results suggest that PC1 mainly represents the boundary

515 layer conditions, and the co-variations of the boundary layer water vapor and turbulence are the most

516 distinct environmental patterns for the selected cloud cases. The PC2 and PC3 are most correlated with

517 LTS (0.58 and 0.65 for PC2 and PC3, respectively) and $W_{dir,NS}$ (0.60 and -0.50 for PC2 and PC3,

518 respectively), indicating that the PC2 and PC3 mainly describe the variations in large-scale

519 thermodynamic and the surface wind patterns, which are likely associated with the variations of the

520 Azores High position and strength (Wood et al., 2015).

521 To further understand the correlations between the meteorological variables, the principal

522 component loadings plot is constructed by projecting the variables onto PC1 and PC2 as shown in Fig.

523 4. Each point denotes the variable correlations with PC1 (x-coordinate) and PC2 (y-coordinate), so that

524 each vector represents the strength and direction of the original variable influences on the pair of PCs.

525 The angle between the two vectors represents the correlation between each other. In Fig. 4, both TKE_w

526 and $W_{dir,NS}$ vectors are located in the same quadrant (positive in both PC1 and PC2) and close to each

527 other with a small degree of an acute angle, which means the TKE_w are strongly correlated with the

528 $W_{dir,NS}$. When the surface wind is coming from the north side of the island, the topographic lifting effect

529 of the cliff would induce additional updraft over the ENA site (Zheng et al., 2016), so that the wind closer

530 to the northerly wind (larger $W_{dir,NS}$) is more correlated with higher TKE_w. Note that TKE_w and D_i

531 vectors are almost in an opposite direction, which denotes a strongly negative correlation between the

532 two variables. The angles of PWV_{BL} with D_i (~45°) and TKE_w (~142°) suggest that PWV_{BL} is

533 moderately positively correlated with D_i but negatively correlated with TKE_w. A higher D_i indicates a

534 more decoupled MBL, where MBL is not well-mixed and separated into a radiative-driven layer and a

535 surface flux driven layer that caps the surface moisture (Jones et al., 2011). This situation is more likely

536 to be associated with a relatively higher PWV_{BL} and weaker TKE_w condition. Note that the negative

539 correlation between D_i and TKE_w examined here might also be partly attributed to the diurnal cycle of
540 the turbulence, which is studied to be associated with the cloud-top longwave radiative cooling over the
541 ENA, especially for the drizzling clouds (Ghate et al., 2021; Zheng et al., 2016). However, this study
542 focuses on the non-precipitating clouds where the effect of drizzle on the cloud-top radiative cooling
543 driven turbulence is minimum, and examining the cloud-top radiative cooling rate from ground-based
544 remote sensing is beyond the scope of the current study. It would be with interest to get the accurate
545 cloud-top radiative cooling rate using a radiative transfer model to perform further study in the future.

546 As for the LTS parameter, the close to 90° angle with TKE_w suggests no correlation between them, since
547 the LTS is mostly capturing the large-scale thermodynamical structures and is obtained from a coarser
548 temporal resolution. Thus, the LTS does not essentially have correspondence to the strength of boundary
549 layer turbulence and can be treated as independent to TKE_w over the ENA site. The loading plot
550 intuitively tells us the directions and strengths of the co-variabilities of the selected meteorological
551 variables, and sheds the light on determining the key factors that are feasible to use in examining the
552 environmental impacts on the aerosol-cloud interactions.

3.5 Linking the meteorological factors to aerosol-cloud interaction

3.5.1 Relations of meteorological factors with aerosol and cloud properties

557 The PCs are, mathematically, the linear combination of the selected variables, and hence independent of
558 each other after the PCA. Therefore, treating the aerosol and cloud properties as dependents and
559 correlated with the PCs allows us to infer their co-variation with the meteorological factors statistically.
560 A weakly negative correlation between $N_{CCN,0.2\%}$ and PC1 ($R_{PC1,CCN} = -0.35$) suggests that the
561 relatively higher $N_{CCN,0.2\%}$ could be sometimes found under higher PWV_{BL} and lower TKE_w. Though
562 the correlation is low, the plausible contributions could come from the seasonal variations of $N_{CCN,0.2\%}$
563 and PWV_{BL} as discussed in the previous section, and the weaker TKE_w might prevent the vertical mixing
564 of CCN and induce higher surface $N_{CCN,0.2\%}$. On the other hand, a weakly positive correlation between
565 $N_{CCN,0.2\%}$ and PC2 ($R_{PC2,CCN} = 0.21$) suggests that there are no fundamental relationships between
566 CCN with thermodynamic and the surface wind direction, and they are not the key controlling factor of
567 surface $N_{CCN,0.2\%}$ variation because the surface CCN concentration is primarily contributed by the
568 accumulation-mode aerosols which come from the condensational growth of Aitken-mode aerosols
569 (Zheng et al., 2018). As for the cloud properties, both N_c and f_{ad} are negatively correlated with PC1
570 ($R_{PC1,Nc} = -0.51$ and $R_{PC1,fad} = -0.62$, respectively), suggesting a moderate relationship between N_c,

571   f_{ad}, and the boundary layer condition. These negative correlations suggest that under the higher PWV_{BL}

572   condition, the sufficient water vapor supply allows more CCN to become cloud droplets, as previously

573   discussed, and hence increases the cloud adiabaticity due to the dominant condensational growth process.

574   While in the situation of relatively higher TKE_w, the decrease in the N_c and f_{ad} might be partly attributed

575   to the association with the active in-cloud coalescence process and entrainment of dry air. However,

576   owing to the obstacle of retrieving in-cloud TKE_w from the ground-based remote sensing, the usage of

577   sub-cloud TKE_w in this study captures part of the relationship between turbulence and adiabaticity.

578   Therefore, in this situation, the cloud adiabaticity might depend more on PWV_{BL} and the boundary layer

579   decoupling state. Moreover, their low correlations with PC2 ($R_{PC2,Nc} = -0.10$ and $R_{PC2,fad} = -0.17$,

580   respectively) indicate very weak relations with the large-scale thermodynamic variables. These weak

581   correlations might likely be due to the subset of MBL single-layer stratocumulus in this study, as the

582   previous study over the ENA found that the sensitivity of MBL cloud adiabaticity largely depends on the

583   strength of cloud top inversion (which can be partially indicated by the increased LTS) and slightly

584   depends on the boundary layer decoupling (Terai et al., 2019; Zheng et al., 2020). Note that the same

585   sign of correlations with PC1 statistically infer the similar directional co-variation of $N_{CCN,0.2\%}$, N_c, and

586   f_{ad} to a certain extent.

587   To examine the physical relation between $N_{CCN,0.2\%}$, N_c and f_{ad}, the profiles of cloud r_e and

588   LWC are plotted in normalized height from cloud base (z_b) to cloud top height (z_t) (Fig. 5), which is

589   given by $z_n = (z - z_b) / (z_t - z_b)$. The solid lines denote the mean values, and the shaded area

590   represents one standard deviation at each normalized height z_n. The normalized r_e increases from ~8.6

591   μm at the cloud base toward ~11 μm near the upper part of the cloud where z_n is 0.7 (Fig. 5a), through

592   condensational growth and coalescence processes, and then decreases toward the cloud top due to cloud-

593   top entrainment. Similar in-cloud vertical variation of r_e is also found by previous study using aircraft

594   in-situ measurements (Zhao et al., 2018; Wu et al. 2020a). Profiles of retrieved LWC and calculated

595   adiabatic LWC_{ad} (blue line) are presented in Fig. 5b. As demonstrated in Fig. 5b, the f_{ad} values, which

596   is the ratio of LWC to LWC_{ad}, reach a maximum of 0.8 at the cloud base and a minimum of 0.38 at the

597   cloud top. The shaded areas of r_e and LWC denote the range from near-adiabatic to sub-adiabatic cloud

598   environments, where in the near-adiabatic cloud (higher f_{ad}) the cloud droplets experience adiabatic

599   growth and LWC should be close to LWC_{ad}. In contrast, in the sub-adiabatic cloud regime, the decrease

600   of f_{ad} is largely due to cloud-top entrainment and coalescence processes even in non-precipitating MBL

601   clouds (Wood, 2012; Braun et al., 2018; Wu et al. 2020b). Furthermore, to understand the implication of

603 cloud adiabaticity with respect to CCN-N_c conversion, all of the f_{ad} samples are separated into two

604 groups by the median value of the layer-mean f_{ad} (0.66) for further analysis.

605   Figure 6 shows N_c against the binned $N_{CCN,0.2\%}$ for the near-adiabatic regime ($f_{ad} > 0.66$) and

606 sub-adiabatic regime ($f_{ad} < 0.66$). For the near-adiabatic regime, N_c increases from ~60 cm^{-3} to 119

607 cm^{-3} with increased $N_{CCN,0.2\%}$ and PWV$_{BL}$, and both $N_{CCN,0.2\%}$ and PWV$_{BL}$ appear to play positive roles

608 in terms of the N_c increase. The result is as expected because the process of condensational growth is

609 predominant in the near-adiabatic clouds, that is, with increasing water vapor supply, the higher CCN

610 loading can effectively lead to more cloud droplets. However, in the sub-adiabatic cloud regime, N_c

611 increases with increased $N_{CCN,0.2\%}$ but possesses a negative correlation with PWV, which results in a

612 slower increase of N_c under higher $N_{CCN,0.2\%}$ and PWV$_{BL}$ conditions. The mean reduction of N_c in the

613 sub-adiabatic regime is computed to be ~37% compared to that for the near-adiabatic clouds. As

614 previously studied, the coalescence process contributes significantly to N_c depletion, even in a non-

615 precipitating MBL clouds (Feingold et al., 1996; Wood, 2006). Thus, lower N_c in the sub-adiabatic

616 regime may be partly due to the combined effect of coalescence and entrainment (Wood, 2006; Hill et

617 al., 2009; Yum et al., 2015; Wang et al., 2020). Note that the retrieved N_c represents the cloud layer-

618 mean information. In summary, the Wu et al. (2020a) retrieval works to separate the reflectivity into the

619 contributions of cloud (Z_c) and drizzle. The retrieval assumes an initial guess of the representative layer-

620 mean N_c based on the climatology over ENA sites (Dong et al., 2014), and such allows the first guess of

621 the vertical profile of LWC based on N_c and Z_c, and then constrains the N_c and LWC using the LWP

622 derived from MWR, and finally output r_e values (Fig. 3 in Wu et al., 2020a). Therefore, the final

623 retrieved N_c is updated to in response to the cloud microphysical processes within this time-step. From

624 the aircraft in-situ measurements during the ACE-ENA, we found that the observed vertical profile of

625 N_c is near-constant in the middle part of the cloud (even in the drizzling cloud where the collision-

626 coalescence processes are more active), and the signal of entrainment-induced N_c depletion is shown

627 near the cloud top (Wu et al., 2020a). However, it is difficult and beyond the scope of the ground-based

628 retrieval to compare the vertical dependency of depletion rate within one time-step. Therefore, as the

629 retrieval currently works to represent the layer-mean information from the given time-step, the preferred

630 method in this study is to compare N_c at different times, where in this case are the adiabatic versus sub-

631 adiabatic conditions which hence yields different N_c that we retrieved from the ground-based snapshot

632 perspective. From the PCA and binning analysis, the effect of cloud adiabaticities on CCN-N_c

633 conversions may shed light on interpreting the aerosol-cloud interaction under different environmental

634 effects.

648

3.5.2 The role of meteorological factors on ACI_r assessment

Since ACI_r can only be calculated by the logarithmic derivatives from a set of $N_{CCN,0.2\%}$ and r_e data within a certain regime, it will be inappropriate to linearly correlate the data with PCs directly, in both mathematical and physical perspectives. Therefore, the meteorological factors which have the strongest influence on the most explanatory PCs, namely PWV_{BL} and TKE_w are selected to be the sorting variables in assessing the environmental impacts on the ACI_r. In addition, LTS is also selected as it represents the large-scale thermodynamic factor and is independent to the boundary-layer environment conditions. The data samples are first separated into two regimes using the median values of the targeting factors, and then separated into four quadrants by the median PWV_{BL} because ACI_r is found to have significant differences under different water vapor availabilities. The ACI_r values are further calculated for all quadrants to examine whether the ACI_r can be distinguished by the targeting factors.

Combining LTS and PWV_{BL} as sorting variables, the ACI_r values for four regimes are shown in Fig. S4. The ACI_r differences between low and high PWV_{BL} regimes are still retained. In the low PWV_{BL} regime, the ACI_r values are limited to 0.016 and 0.056 for low and high LTS regimes, respectively. In the high PWV_{BL} regime, the ACI_r values are 0.150 and 0.171 for low and high LTS regimes, respectively, which is about 3-5 times greater than those in low PWV_{BL} regime. However, the ACI_r in different LTS regimes cannot be distinctly differentiated (ACI_r differences between LTS regimes are ~0.02 and ~0.04), and the main difference in ACI_r are still induced by the PWV_{BL}. Owing to the location of the ENA site where it locates near the boundary of mid-latitude and subtropical climate regimes, the MBL clouds over the ENA are found to be often under the influences of cold fronts associated with mid-latitude cyclones, where the cloud evolutions are subject to the combine effects of post-frontal and large-scale subsidence (Wood et al., 2015; Zheng et al., 2020; Wang et al., 2021). Therefore, over the ENA, although the spatial gradient of LTS is studied to be associated with the production of MBL turbulence and the change in wind direction (Wu et al., 2017), the LTS value itself is examined to have a weak impact on the aerosol-cloud interaction from this study.

The TKE_w has been found to be strongly positively correlated with $W_{dir,NS}$ and negatively correlated with D_i from the PCA, that is, the values of TKE_w already account for the co-variabilities in these variables. Therefore, treating TKE_w as the sorting variable would lead to a more physical process-orientated assessment. Accordingly, to examine the role of the dynamical factors on ACI, the samples are separated into four regimes demarcated by the median values of PWV_{BL} and TKE_w (Fig. 7), and the mean values of D_i and f_{ad} in the four quadrants are also displayed in Fig. 7. The effect of PWV_{BL} on

681   ACI_r is demonstrated by the mean ACI_r values where they are much higher in the high PWV_{BL} regime

682   than those in the low PWV_{BL} regime no matter what the TKE_w regimes. Furthermore, the result illustrates

683   that TKE_w does play an important role in ACI_r, because the ACI_r values in the high TKE_w regime are

684   more than double than the values in the low TKE_w regime.

685   In the regimes of high TKE_w and PWV_{BL}, which are closely associated with coupled MBL ($D_i =$

686   0.21) and more sub-adiabatic cloud conditions ($f_{ad} = 0.52$), r_e is highly sensitive to CCN loading with

687   the highest ACI_r of 0.259. The sufficient water vapor availability allows CCN to be converted into cloud

688   droplets more effectively, while the relatively higher TKE_w indicates stronger turbulence in the below-

689   cloud boundary layer and maintains a nearly well-mixed MBL. The CCN and moisture below-cloud layer

690   are efficiently transported and mixed aloft via the ascending branch of the eddies (Nicholls, 1984; Hogan

691   et al., 2009), hence are effectively connected to the cloud layer. Therefore, under the lower CCN loading

692   condition, the active coalescence process (which indicated by the low f_{ad} values) results in the depletion

693   of small cloud droplets and broadening of cloud DSD (Chandrakar et al., 2016), and in turn, leads to

694   further enlarged r_e. However, with higher CCN intrusion into the cloud layer, the enhanced cloud droplet

695   conversion and the subsequential condensational growth behave contradictorily to narrow the DSD

696   (Pinsky and Khain, 2002; Pawlowska et al., 2006), which leads to decreased r_e. Therefore, the MBL

697   clouds are distinctly susceptible to CCN loading under the environments of sufficient water vapor and

698   strong turbulence in which the ACI_r is enlarged.

699   Under high PWV_{BL} but low TKE_w conditions, the mean ACI_r reduces to 0.101 (~ 39% of that

700   under high TKE_w). The MBL is more likely decoupled where $D_i = 0.54$, which indicates that the weaker

701   turbulence loosens the connection between the cloud layer and the underlying boundary layer. This

702   results in a less effective conversion of CCN into cloud droplets, while the more adiabatic cloud

703   environment ($f_{ad} = 0.75$) denotes the lack of coalescence growths and thus diminishes the r_e sensitivity

704   to CCN. Although the constraints of insufficient water vapor on ACI_r are still evident, the ACI_r values

705   increase from 0.008 in the low TKE_w regime to 0.024 in the high TKE_w regime. The ACI_r differences

706   between the two TKE_w regimes attest that ACI_r strongly depends on the connection between the cloud

707   layer and the below-cloud boundary layer CCN and moisture, that is, stronger turbulence can enhance

708   the susceptibility of r_e to CCN.

709   In this study, the relationship between turbulence and ACI is found to be valid in non-precipitating

710   MBL clouds. Theoretically, the effect of turbulence on ACI_r would appear to be artificially amplified, if

711   in the presence of precipitation. The intensive turbulence can enhance the coalescence process and

712   accelerate the CCN-cloud cycling, and subsequently, the CCN depletion due to precipitation and

713 coalescence scavenging would result in quantitatively enlarged ACI_r (Feingold et al., 1996, 1999; Duong
714 et al., 2011; Braun et al., 2018). Though it is beyond the scope of this study, it would be of interest to
715 perform such analysis on the aerosol-cloud-precipitation interaction using ground-based remote sensing
716 and model simulations in a future study.

717

4. Summaries and Conclusions

719 Over the ARM-ENA site, a total of 20 non-precipitating single-layered MBL stratus and
720 stratocumulus cloud cases have been selected in order to investigate the aerosol-cloud interaction (ACI).
721 The distributions of CCN and cloud properties for selected cases represent the typical characteristics of
722 non-precipitating MBL clouds in a relatively clean environment over the remote oceanic area. The
723 diversity of boundary layer conditions and cloud adiabaticities among the selected cases enable the
724 investigation of different environmental effects on ACI.

725 The overall variations of N_c with $N_{CCN,0.2\%}$ show an increasing trend, regardless of the water vapor
726 condition, while the sufficient PWV_{BL} appears to stabilize the CCN-N_c conversion process. The water
727 vapor limitation on cloud droplet growth is evident in the lower $N_{CCN,0.2\%}$ up to 150 cm^{-3} with low
728 PWV_{BL} values, where a near tripling of CCN loading leads to a near doubling of N_c but only 4.7%
729 increase in r_e. When $N_{CCN,0.2\%}$ is greater than 250 cm^{-3} and PWV_{BL} values are also relatively high, r_e
730 appears to decrease with increasing $N_{CCN,0.2\%}$ under similar water vapor conditions. As for bulk aerosol-
731 cloud interaction, the ACI_r values vary from -0.01 to 0.22 for different PWV_{BL} conditions where ACI_r
732 appears to be diminished under limited water vapor availability due to limited droplet activation and
733 condensational growth processes. While under relatively sufficient water supply conditions, r_e shows
734 more sensitive responses to the changes of $N_{CCN,0.2\%}$, due to the combined effect of condensational
735 growth and coalescence processes accompanying the higher N_c and PWV_{BL}.

736 The theoretical diagram describing the mechanism proposed above is shown in Fig. 8. Under the
737 relatively lower PWV_{BL} condition, the limited water vapor weakens the ability of condensational growth
738 of the cloud droplet converted from CCN, which results in both less newly converted as well as large
739 cloud droplets, with the lack of chance of coalescence processes under this circumstance. Therefore, the
740 variable range of r_e versus $N_{CCN,0.2\%}$ is narrowed and presented as small ACI_r. While under the relatively
741 higher PWV_{BL} condition, particularly in low CCN conditions, the sufficient water vapor availability
742 allows cloud droplets growing via the condensation of water vapor, and thus enter the active cloud-
743 droplet coalescence regime. In contrast, the increase in cloud droplet size can effectively reduce N_c via
744 the coalescence process and the size distributions are effectively broadened toward the large tail by the

751 coalescence, so that r_e is enlarged. Under a higher $N_{CCN,0.2\%}$ intrusion, the cloud droplet size distribution
752 is narrowed by the enhanced condensational growth and regresses toward the small tail by increasing the
753 amount of newly converted cloud droplets which results in decreased r_e. Combinedly, the interactions
754 between CCNs and cloud droplet growth processes ultimately result in a broadened changeable range of

755 r_e, and in turn, the enlarged ACI_r.

756   The co-variabilities among the environmental factors are examined using the multi-dimensional
757 PCA. The variables of PWV_{BL}, D_i, TKE_w, LTS and $W_{dir,NS}$ are constructed as the input of the
758 eigenanalysis. Results show that the first three PCs can describe the majority (~84%) of the variance
759 among the selected variables. The most explanatory PC1 (account for 43.72% contribution) strongly
760 correlated with PWV_{BL}, D_i (both negatively) and TKE_w (positively), and hence describe the co-variation
761 of the boundary layer conditions. While the PC2 and PC3 (account for 22.01% and 18.26% contributions,
762 respectively) are strongly correlated with LTS and $W_{dir,NS}$, which likely indicates the variations of the
763 Azores High position and strength. By projecting the variables onto PC1 and PC2, the PCA loading
764 analysis shows that TKE_w is strongly negatively correlated with D_i, which is what we expected. A
765 decoupled MBL cloud is often separated into two layers where the lower one can cap the surface moisture,
766 while the higher TKE_w denote sufficient turbulence that maintains the well-mixed MBL. Additionally,
767 the island effect is also indicated by the eigenanalysis, where surface northerly wind would induce
768 additional updraft velocity and hence disturb TKE_w, owing to the effect of the cliff north of the ENA site.

769 The role of cloud adiabaticities on the behaviors of CCN-N_c conversion is examined using both binning
770 and eigenanalysis. In a near-adiabatic cloud vertical structure, the cloud droplet growth process is

771 dominated by condensational growth, thus the N_c responses to increased $N_{CCN,0.2\%}$ and PWV_{BL} are
772 strengthened. When the cloud layer becomes more sub-adiabatic, the effect of coalescence leads to the
773 depletion of N_c and thus results in the lower retrieved N_c from a ground-based snapshot perspective. The
774 competition between the condensational growth and coalescence processes strongly impacts the
775 variations of cloud microphysics to CCN loading.

776   To investigate the environmental effects on ACI_r, the factors having the most influence on the
777 explanatory PCs are selected as the sorting variables in the ACI_r assessments. The LTS sorting method
778 cannot distinguish the ACI_r values, which means the LTS values themselves have a weak impact on ACI_r
779 due to the MBL cloud cover over the ENA is mainly impacted by the mid-latitude cyclone systems. In
780 contrast, the intensity of boundary layer turbulence represented by TKE_w plays a more important role in
781 ACI_r, since the values of TKE_w already account for the co-variations of the MBL conditions, and hence
782 leads to a physical process-orientated assessment. The ACI_r assessments in four different TKE_w and

786   PWV$_{BL}$ regimes show that the constraints of insufficient water vapor on the ACI$_r$ are still evident, but in
787   both PWV$_{BL}$ regimes the ACI$_r$ values increase more than double from low TKE$_w$ to high TKE$_w$ regimes.
788   Noticeably, the ACI$_r$ increases from 0.101 in the low TKE$_w$ regime to 0.259 in the high TKE$_w$ regime,
789   under high PWV$_{BL}$ conditions. The intensive below-cloud boundary layer turbulence strengthens the
790   connection between the cloud layer and below-cloud CCN and moisture. So that with sufficient water
791   vapor, an active coalescence leads to further enlarged r_e, particularly for low CCN loading conditions,
792   while the enhanced N_c from condensational growth induced by increased $N_{CCN,0.2\%}$ can effectively
793   decrease r_e. Combining these processes together, the enlarged ACI$_r$ is presented.

794   In this study, the non-precipitating MBL clouds are found to be most susceptible to the below-cloud
795   CCN loading under environments with sufficient water vapor and stronger turbulence. This study
796   examines the importance of the environmental effects on the ACI$_r$ assessments, and provides the
797   observational constraints to the future model evaluations on the aerosol-cloud interactions. Future studies
798   will be focusing on exploring the role of environmental effects on the aerosol-cloud-precipitation
799   interactions in MBL stratocumulus through an integrative analysis of observations and model simulations.
800
801
802   *Data availability.* Data used in this study can be accessed from the DOE ARM's Data Discovery at
803   https://adc.arm.gov/discovery/
804
805   *Author contributions.* The original idea of this study is discussed by XZ, BX, and XD. XZ performed the
806   analyses and wrote the manuscript. XZ, BX, XD, PW, YW and TL participated in further scientific
807   discussions and provided substantial comments and edits on the paper.
808
809   *Competing interests.* The authors declare that they have no conflict of interest.
810
811   *Special issue statement.* This article is part of the special issue "Marine aerosols, trace gases, and clouds
812   over the North Atlantic (ACP/AMT inter-journal SI)". It is not associated with a conference.
813

814   *Acknowledgments.* The ground-based measurements were obtained from the Atmospheric Radiation
815   Measurement (ARM) Program sponsored by the U.S. Department of Energy (DOE) Office of Energy
816   Research, Office of Health and Environmental Research, and Environmental Sciences Division. The
817   reanalysis data were obtained from the ECMWF model output, which provides explicitly for the analysis
818   at the ARM ENA site. The data can be downloaded from https://adc.arm.gov/discovery/. This work was

820 supported by the NSF grants AGS-1700728/1700727 and AGS-2031750/2031751, and was also
821 supported as part of the "Enabling Aerosol-cloud interactions at GLobal convection-permitting scalES
822 (EAGLES)" project (74358), funded by the U.S. Department of Energy, Office of Science, Office of
823 Biological and Environmental Research, Earth System Modeling program with the subcontract to the
824 University of Arizona. The Pacific Northwest National Laboratory is operated for the Department of
825 Energy by Battelle Memorial Institute under Contract DE-AC05-76 RL01830. And a special thanks to
826 coeditor Dr. Hang Su and three anonymous reviewers for the constructive comments and suggestions,
827 which helped to improve the manuscript.

828

829 **References.**

830 Albrecht, B. A., Bretherton, C. S., Johnson, D., Schubert, W. H. and Frisch, A. S.: The Atlantic
831   Stratocumulus Transition Experiment - ASTEX, Bull. - Am. Meteorol. Soc., doi:10.1175/1520-
832   0477(1995)076<0889:TASTE>2.0.CO;2, 1995.

833 ARM MET Handbook: ARM Surface Meteorology Systems (MET) Handbook, DOE ARM Climate
834   Research Facility, DOE/SC-ARM/TR-086. Available at:
835   https://www.arm.gov/publications/tech_reports/handbooks/met_handbook.pdf, last access: 21
836   August 2021.

837 Braun, R. A., Dadashazar, H., MacDonald, A. B., Crosbie, E., Jonsson, H. H., Woods, R. K., Flagan, R.
838   C., Seinfeld, J. H. and Sorooshian, A.: Cloud Adiabaticity and Its Relationship to Marine
839   Stratocumulus Characteristics Over the Northeast Pacific Ocean, J. Geophys. Res. Atmos.,
840   doi:10.1029/2018JD029287, 2018.

841 Cadeddu, M. P., Liljegren, J. C. and Turner, D. D.: The atmospheric radiation measurement (ARM)
842   program network of microwave radiometers: Instrumentation, data, and retrievals, Atmos. Meas.
843   Tech., doi:10.5194/amt-6-2359-2013, 2013.

844 Chandrakar, K. K., Cantrell, W., Chang, K., Ciochetto, D., Niedermeier, D., Ovchinnikov, M., Shaw, R.
845   A. and Yang, F.: Aerosol indirect effect from turbulence-induced broadening of cloud-droplet size
846   distributions, Proc. Natl. Acad. Sci. U. S. A., doi:10.1073/pnas.1612686113, 2016.

847 Chen, Y. C., Christensen, M. W., Stephens, G. L. and Seinfeld, J. H.: Satellite-based estimate of global

848   aerosol-cloud radiative forcing by marine warm clouds, Nat. Geosci., doi:10.1038/ngeo2214, 2014.

849 Costantino, L. and Bréon, F. M.: Analysis of aerosol-cloud interaction from multi-sensor satellite

850   observations, Geophys. Res. Lett., doi:10.1029/2009GL041828, 2010.

851 Diamond, M. S., Dobracki, A., Freitag, S., Griswold, J. D. S., Heikkila, A., Howell, S. G., Kacarab, M.

852   E., Podolske, J. R., Saide, P. E. and Wood, R.: Time-dependent entrainment of smoke presents an

853   observational challenge for assessing aerosol-cloud interactions over the southeast Atlantic Ocean,

854   Atmos. Chem. Phys., doi:10.5194/acp-18-14623-2018, 2018.

855 Dong, X., Xi, B., Kennedy, A., Minnis, P. and Wood, R.: A 19-month record of marine aerosol-cloud-

856   radiation properties derived from DOE ARM mobile facility deployment at the Azores. Part I: Cloud

857   fraction and single-layered MBL cloud properties, J. Clim., doi:10.1175/JCLI-D-13-00553.1, 2014.

858 Dong, X., Schwantes, A. C., Xi, B. and Wu, P.: Investigation of the marine boundary layer cloud and

859   CCN properties under coupled and decoupled conditions over the azores, J. Geophys. Res.,

860   doi:10.1002/2014JD022939, 2015.

861 Duong, H. T., Sorooshian, A. and Feingold, G.: Investigating potential biases in observed and modeled

862   metrics of aerosol-cloud-precipitation interactions, Atmos. Chem. Phys., doi:10.5194/acp-11-4027-

863   2011, 2011.

864 Fan, J., Wang, Y., Rosenfeld, D., Liu, X.: Review of Aerosol-Cloud Interactions: Mechanisms,

865   Significance and Challenges, J. Atmo. Sci. 73(11), 4221-4252, 2016.

866 Feingold, G., Kreidenweis, S. M., Stevens, B. and Cotton, W. R.: Numerical simulations of stratocumulus

867   processing of cloud condensation nuclei through collision-coalescence, J. Geophys. Res. Atmos.,

868   doi:10.1029/96jd01552, 1996.

869 Feingold, G., Frisch, A. S., Stevens, B. and Cotton, W. R.: On the relationship among cloud turbulence,

870   droplet formation and drizzle as viewed by Doppler radar, microwave radiometer and lidar, J.

871   Geophys. Res. Atmos., doi:10.1029/1999JD900482, 1999.

872 Feingold, G., Furrer, R., Pilewskie, P., Remer, L. A., Min, Q. and Jonsson, H.: Aerosol indirect effect
873   studies at Southern Great Plains during the May 2003 Intensive Operations Period, J. Geophys. Res.
874   Atmos., doi:10.1029/2004JD005648, 2006.

875 Feingold, G. and McComiskey, A.: ARM's Aerosol–Cloud–Precipitation Research (Aerosol Indirect
876   Effects), Meteorol. Monogr., doi:10.1175/amsmonographs-d-15-0022.1, 2016.

877 Freud, E. and Rosenfeld, D.: Linear relation between convective cloud drop number concentration and
878   depth for rain initiation, J. Geophys. Res. Atmos., doi:10.1029/2011JD016457, 2012.

879 Garrett, T. J. and Zhao, C.: Increased Arctic cloud longwave emissivity associated with pollution from
880   mid-latitudes, Nature, doi:10.1038/nature04636, 2006.

881 Garrett, T. J., Zhao, C., Dong, X., Mace, G. G. and Hobbs, P. V.: Effects of varying aerosol regimes on
882   low-level Arctic stratus, Geophys. Res. Lett., doi:10.1029/2004GL019928, 2004.

883 Gerber, H.: Microphysics of marine stratocumulus clouds with two drizzle modes, J. Atmos. Sci.,
884   doi:10.1175/1520-0469(1996)053<1649:MOMSCW>2.0.CO;2, 1996.

885 Ghate, V. P., Albrecht, B. A. and Kollias, P.: Vertical velocity structure of nonprecipitating continental
886   boundary layer stratocumulus clouds, J. Geophys. Res. Atmos., doi:10.1029/2009JD013091, 2010.

887 Ghate, V. P. and Cadeddu, M. P.: Drizzle and Turbulence Below Closed Cellular Marine Stratocumulus
888   Clouds, J. Geophys. Res. Atmos., doi:10.1029/2018JD030141, 2019.

889 Ghate, V. P., Cadeddu, M. P., Zheng, X. and O'Connor, E.: Turbulence in The Marine Boundary Layer
890   and Air Motions Below Stratocumulus Clouds at the ARM Eastern North Atlantic Site, J. Appl.
891   Meteorol. Climatol., doi:10.1175/jamc-d-21-0087.1, 2021.

892 Gryspeerdt, E., Quaas, J. and Bellouin, N.: Constraining the aerosol influence on cloud fraction, J.
893   Geophys. Res., doi:10.1002/2015JD023744, 2016.

894 Hill, A. A., Feingold, G. and Jiang, H.: The influence of entrainment and mixing assumption on aerosol–
895   cloud interactions in marine stratocumulus, J. Atmos. Sci., doi: 10.1175/2008JAS2909.1, 2009.

Formatted: Font: Liberation Serif

896 Hogan, R. J., Grant, A. L. M., Illingworth, A. J., Pearson, G. N. and O'Connor, E. J.: Vertical velocity

897   variance and skewness in clear and cloud-topped boundary layers as revealed by Doppler lidar, Q.

898   J. R. Meteorol. Soc., doi:10.1002/qj.413, 2009.

899 Hudson, J. G. and Noble, S.: CCN and Vertical Velocity Influences on Droplet Concentrations and

900   Supersaturations in Clean and Polluted Stratus Clouds, J. Atmos. Sci., doi:10.1175/jas-d-13-086.1,

901   2013.

902 Jones, C. R., Bretherton, C. S., and Leon, D.: Coupled vs. decoupled boundary layers in VOCALS-REx,

903   Atmos. Chem. Phys., 11, 7143–7153, https://doi.org/10.5194/acp-11-7143-2011, 2011.

904 Klein, S. A. and Hartmann, D. L.: The seasonal cycle of low stratiform clouds, J. Clim.,

905   doi:10.1175/1520-0442(1993)006<1587:TSCOLS>2.0.CO;2, 1993.

906 Kim, B. G., Miller, M. A., Schwartz, S. E., Liu, Y. and Min, Q.: The role of adiabaticity in the aerosol

907   first indirect effect, J. Geophys. Res. Atmos., doi:10.1029/2007JD008961, 2008.

908 Liu, J., Li, Z. and Cribb, M.: Response of marine boundary layer cloud properties to aerosol perturbations

909   associated with meteorological conditions from the 19-month AMF-Azores campaign, J. Atmos.

910   Sci., doi:10.1175/JAS-D-15-0364.1, 2016.

911 Lappen, C. L. and Randall, D. A.: Toward a unified parameterization of the boundary layer and moist

912   convection. Part I: A new type of mass-flux model, J. Atmos. Sci., doi:10.1175/1520-

913   0469(2001)058<2021:TAUPOT>2.0.CO;2, 2001.

914 Logan, T., Xi, B. and Dong, X.: Aerosol properties and their influences on marine boundary layer cloud

915   condensation nuclei at the ARM mobile facility over the Azores, J. Geophys. Res.,

916   doi:10.1002/2013JD021288, 2014.

917 Logan, T., Dong, X. and Xi, B.: Aerosol properties and their impacts on surface CCN at the ARM

918   Southern Great Plains site during the 2011 Midlatitude Continental Convective Clouds Experiment,

919   Adv. Atmos. Sci., doi:10.1007/s00376-017-7033-2, 2018.

920   Lu, M. L., Conant, W. C., Jonsson, H. H., Varutbangkul, V., Flagan, R. C. and Seinfeld, J. H.: The marine

921   stratus/stratocumulus experiment (MASE): Aerosol-cloud relationships in marine stratocumulus, J.

922   Geophys. Res., doi:10.1029/2006JD007985, 2007.

923   Mann, J. A., Christine Chiu, J., Hogan, R. J., O'Connor, E. J., L'Ecuyer, T. S., Stein, T. H. and Jefferson,

924   A.: Aerosol impacts on drizzle properties in warm clouds from ARM Mobile Facility maritime and

925   continental deployments, J. Geophys. Res., doi:10.1002/2013JD021339, 2014.

926   Martin, G. M., Johnson, D. W. and Spice, A.: The Measurement and Parameterization of Effective Radius

927   of Droplets in Warm Stratocumulus Clouds, J. Atmos. Sci., doi:10.1175/1520-

928   0469(1994)051<1823:tmapoe>2.0.co;2, 1994.

929   Martins, J. V., Marshak, A., Remer, L. A., Rosenfeld, D., Kaufman, Y. J., Fernandez-Borda, R., Koren,

930   I., Correia, A. L., Zubko, V. and Artaxo, P.: Remote sensing the vertical profile of cloud droplet

931   effective radius, thermodynamic phase, and temperature, Atmos. Chem. Phys., doi:10.5194/acp-11-

932   9485-2011, 2011.

933   McComiskey, A, Feingold, G., Frisch, A. S., Turner, D. D., Miller, M., Chiu, J. C., Min, Q. and Ogren,

934   J.: An assessment of aerosol-cloud interactions in marine stratus clouds based on surface remote

935   sensing, J. Geophys. Res., 114, D09203, doi:10.1029/2008JD011006, 2009.

936   McComiskey, A. and Feingold, G.: The scale problem in quantifying aerosol indirect effects, Atmos.

937   Chem. Phys., doi:10.5194/acp-12-1031-2012, 2012.

938   Medeiros, B. and Stevens, B.: Revealing differences in GCM representations of low clouds, Clim. Dyn.,

939   doi:10.1007/s00382-009-0694-5, 2011.

940   Morris, V. R.: Ceilometer Instrument Handbook, DOE ARM Climate Research Facility, DOE/SC-ARM-

941   TR-020, 2016. Available at:

942   https://www.arm.gov/publications/tech_reports/handbooks/ceil_handbook.pdf, last access: 23

943   April 2021.

944   Newsom, R. K., Sivaraman, C., Shippert, T.R. and Riihimaki, L. D.: Doppler Lidar Vertical Velocity

945   Statistics Value-Added Product. DOE ARM Climate Research Facility, DOE/SC-ARM/TR-149,

2019. Available at: https://www.arm.gov/publications/tech_reports/doe-sc-arm-tr-149.pdf, last access: 2 September 2021.

Nicholls, S.: The dynamics of stratocumulus: Aircraft observations and comparisons with a mixed layer model, Q. J. R. Meteorol. Soc., doi:10.1002/qj.49711046603, 1984.

Pandithurai, G., Takamura, T., Yamaguchi, J., Miyagi, K., Takano, T., Ishizaka, Y., Dipu, S. and Shimizu, A.: Aerosol effect on cloud droplet size as monitored from surface-based remote sensing over East China Sea region, Geophys. Res. Lett., doi:10.1029/2009GL038451, 2009.

Pawlowska, H., Grabowski, W. W. and Brenguier, J. L.: Observations of the width of cloud droplet spectra in stratocumulus, Geophys. Res. Lett., doi:10.1029/2006GL026841, 2006.

Pearson, G., Davies, F. and Collier, C.: An analysis of the performance of the UFAM pulsed Doppler lidar for observing the boundary layer, J. Atmos. Ocean. Technol., doi:10.1175/2008JTECHA1128.1, 2009.

Pinsky, M. B. and Khain, A. P.: Effects of in-cloud nucleation and turbulence on droplet spectrum formation in cumulus clouds, Q. J. R. Meteorol. Soc., doi:10.1256/003590002321042072, 2002.

Qiu, Y., Zhao, C., Guo, J. and Li, J.: 8-Year ground-based observational analysis about the seasonal variation of the aerosol-cloud droplet effective radius relationship at SGP site, Atmos. Environ., doi:10.1016/j.atmosenv.2017.06.002, 2017.

Romps, D. M.: Exact expression for the lifting condensation level, J. Atmos. Sci., doi:10.1175/JAS-D-17-0102.1, 2017.

Rosenfeld, D. and Woodley, W. L.: Closing the 50-year circle: From cloud seeding to space and back to climate change through precipitation physics. Chapter 6 of "Cloud Systems, Hurricanes, and the Tropical Rainfall Measuring Mission (TRMM)", edited by: Tao, W.-K. and Adler, R. F., Meteor. Monogr., 51, 234 pp., 59–80, AMS, 2003.

Rosenfeld, D.: Aerosol-Cloud Interactions Control of Earth Radiation and Latent Heat Release Budgets, in Solar Variability and Planetary Climates., 2007.

971   Rosenfeld, D., Wang, H. and Rasch, P. J.: The roles of cloud drop effective radius and LWP in

972   determining rain properties in marine stratocumulus, Geophys. Res. Lett.,

973   doi:10.1029/2012GL052028, 2012.

974   Rosenfeld, D., Zhu, Y., Wang, M., Zheng, Y., Goren, T. and Yu, S.: Aerosol-driven droplet

975   concentrations dominate coverage and water of oceanic low-level clouds, Science (80-.).,

976   doi:10.1126/science.aav0566, 2019.

977   Seinfeld, J. H., Bretherton, C., Carslaw, K. S., Coe, H., DeMott, P. J., Dunlea, E. J., Feingold, G., Ghan,

978   S., Guenther, A. B., Kahn, R., Kraucunas, I., Kreidenweis, S. M., Molina, M. J., Nenes, A., Penner,

979   J. E., Prather, K. A., Ramanathan, V., Ramaswamy, V., Rasch, P. J., Ravishankara, A. R., Rosenfeld,

980   D., Stephens, G. and Wood, R.: Improving our fundamental understanding of the role of aerosol-

981   cloud interactions in the climate system, Proc. Natl. Acad. Sci. U. S. A.,

982   doi:10.1073/pnas.1514043113, 2016.

983   Siebert, H., Szodry, K.-E., Egerer, U., Wehner, B., Henning, S., Chevalier, K., Lückerath, J., Welz, O.,

984   Weinhold, K., Lauermann, F., Gottschalk, M., Ehrlich, A., Wendisch, M., Fialho, P., Roberts, G.,

985   Allwayin, N., Schum, S., Shaw, R. A., Mazzoleni, C., Mazzoleni, L., Nowak, J. L., Malinowski, S.

986   P., Karpinska, K., Kumala, W., Czyzewska, D., Luke, E. P., Kollias, P., Wood, R. and Mellado, J.

987   P.: Observations of Aerosol, Cloud, Turbulence, and Radiation Properties at the Top of the Marine

988   Boundary Layer over the Eastern North Atlantic Ocean: The ACORES Campaign, Bull. Am.

989   Meteorol. Soc., doi:10.1175/bams-d-19-0191.1, 2021.

990   Terai, C. R., Zhang, Y., Klein, S. A., Zelinka, M. D., Chiu, J. C. and Min, Q.: Mechanisms Behind the

991   Extratropical Stratiform Low-Cloud Optical Depth Response to Temperature in ARM Site

992   Observations, J. Geophys. Res. Atmos., doi:10.1029/2018JD029359, 2019.

993   Thorsen, T. J. and Fu, Q.: Automated retrieval of cloud and aerosol properties from the ARM Raman

994   Lidar. Part II: Extinction, J. Atmos. Ocean. Technol., doi:10.1175/JTECH-D-14-00178.1, 2015.

995   Toto, T, and Jensen, M: Interpolated Sounding and Gridded Sounding Value-Added Products. DOE
996   ARM Climate Research Facility, DOE/SC-ARM-TR-183, 2016. Available at:
997   https://www.arm.gov/publications/tech_reports/doe-sc-arm-tr-183.pdf, last access: 2 September
998   2021.

999   Twohy, C. H., Petters, M. D., Snider, J. R., Stevens, B., Tahnk, W., Wetzel, M., Russell, L. and Burnet,
1000   F.: Evaluation of the aerosol indirect effect in marine stratocumulus clouds: Droplet number, size,
1001   liquid water path, and radiative impact, J. Geophys. Res. D Atmos., doi:10.1029/2004JD005116,
1002   2005.

1003   Twomey, S.: The nuclei of natural cloud formation part II: The supersaturation in natural clouds and the
1004   variation of cloud droplet concentration, Geofis. Pura e Appl., doi:10.1007/BF01993560, 1959.

1005   Twomey, S.: The Influence of Pollution on the Shortwave Albedo of Clouds, J. Atmos. Sci.,
1006   doi:10.1175/1520-0469(1977)034<1149:TIOPOT>2.0.CO;2, 1977.

1007   Wang, Y., Jiang, J.H., Su, H., Choi, S., Huang, L., Guo, J., and Yung, Y. L.: Elucidating the Role of
1008   Anthropogenic Aerosols In Arctic Sea Ice Variations, J. Climate 31(1), 99-114, 2018.

1009   Wang, Y., Zheng, X., Dong, X., Xi, B., Wu, P., Logan, T., and Yung, Y. L.: Impacts of long-range
1010   transport of aerosols on marine-boundary-layer clouds in the eastern North Atlantic, Atmos. Chem.
1011   Phys., 20, 14741–14755, https://doi.org/10.5194/acp-20-14741-2020, 2020.

1012   West, R. E. L., Stier, P., Jones, A., Johnson, C. E., Mann, G. W., Bellouin, N., Partridge, D. G. and
1013   Kipling, Z.: The importance of vertical velocity variability for estimates of the indirect aerosol
1014   effects, Atmos. Chem. Phys., doi:10.5194/acp-14-6369-2014, 2014.

1015   Widener, K, Bharadwaj, N, and Johnson, K: Ka-Band ARM Zenith Radar (KAZR) Instrument Handbook.
1016   DOE ARM Climate Research Facility, DOE/SC-ARM/TR-106, 2012. Available at:
1017   https://www.arm.gov/publications/tech_reports/handbooks/kazr_handbook.pdf, last access: 23
1018   April 2021.

1019   Wood, R.: Rate of loss of cloud droplets by coalescence in warm clouds, J. Geophys. Res. Atmos.,

1020   doi:10.1029/2006JD007553, 2006.

1021   Wood, R. and Bretherton, C. S.: On the relationship between stratiform low cloud cover and lower-

1022   tropospheric stability, J. Clim., doi:10.1175/JCLI3988.1, 2006.

1023   Wood, R.: Stratocumulus clouds, Mon. Weather Rev., doi:10.1175/MWR-D-11-00121.1, 2012.

1024   Wood, R., Wyant, M., Bretherton, C. S., Rémillard, J., Kollias, P., Fletcher, J., Stemmler, J., De Szoeke,

1025   S., Yuter, S., Miller, M., Mechem, D., Tselioudis, G., Chiu, J. C., Mann, J. A. L., O'Connor, E. J.,

1026   Hogan, R. J., Dong, X., Miller, M., Ghate, V., Jefferson, A., Min, Q., Minnis, P., Palikonda, R.,

1027   Albrecht, B., Luke, E., Hannay, C. and Lin, Y.: Clouds, aerosols, and precipitation in the marine

1028   boundary layer: An arm mobile facility deployment, Bull. Am. Meteorol. Soc., doi:10.1175/BAMS-

1029   D-13-00180.1, 2015.

1030   Wu, P., Dong, X. and Xi, B.: Marine boundary layer drizzle properties and their impact on cloud property

1031   retrieval, Atmos. Meas. Tech., doi:10.5194/amt-8-3555-2015, 2015.

1032   Wu, P., Dong, X., Xi, B., Liu, Y., Thieman, M. and Minnis, P.: Effects of environment forcing on marine

1033   boundary layer cloud-drizzle processes, J. Geophys. Res., doi:10.1002/2016JD026326, 2017.

1034   Wu, P., Dong, X., Xi, B., Tian, J. and Ward, D. M.: Profiles of MBL Cloud and Drizzle Microphysical

1035   Properties Retrieved From Ground-Based Observations and Validated by Aircraft In Situ

1036   Measurements Over the Azores, J. Geophys. Res. Atmos., doi:10.1029/2019JD032205, 2020a.

1037   Wu, P., Dong, X. and Xi, B.: A climatology of marine boundary layer cloud and drizzle properties

1038   derived from ground-based observations over the azores, J. Clim., doi:10.1175/JCLI-D-20-0272.1,

1039   2020b.

1040   Xi, B., Dong, X., Minnis, P. and Khaiyer, M. M.: A 10 year climatology of cloud fraction and vertical

1041   distribution derived from both surface and GOES observations over the DOE ARM SPG site, J.

1042   Geophys. Res. Atmos., doi:10.1029/2009JD012800, 2010.

1043   Yang, Y., Zhao, C., Dong, X., Fan, G., Zhou, Y., Wang, Y., Zhao, L., Lv, F. and Yan, F.: Toward
1044   understanding the process-level impacts of aerosols on microphysical properties of shallow cumulus
1045   cloud using aircraft observations, Atmos. Res., doi:10.1016/j.atmosres.2019.01.027, 2019.

1046   Yue, Q., Kahn, B. H., Fetzer, E. J. and Teixeira, J.: Relationship between marine boundary layer clouds
1047   and lower tropospheric stability observed by AIRS, CloudSat, and CALIOP, J. Geophys. Res.
1048   Atmos., doi:10.1029/2011JD016136, 2011.

1049   Yum, S. S., Wang, J., Liu, Y., Senum, G., Springston, S., McGraw, R. and Yeom, J. M.: Cloud
1050   microphysical relationships and their implication on entrainment and mixing mechanism for the
1051   stratocumulus clouds measured during the VOCALS project, J. Geophys. Res.,
1052   doi:10.1002/2014JD022802, 2015.

1053   Zhang, S., Wang, M., J. Ghan, S., Ding, A., Wang, H., Zhang, K., Neubauer, D., Lohmann, U., Ferrachat,
1054   S., Takeamura, T., Gettelman, A., Morrison, H., Lee, Y., T. Shindell, D., G. Partridge, D., Stier, P.,
1055   Kipling, Z. and Fu, C.: On the characteristics of aerosol indirect effect based on dynamic regimes
1056   in global climate models, Atmos. Chem. Phys., doi:10.5194/acp-16-2765-2016, 2016.

1057   Zhao, C., Qiu, Y., Dong, X., Wang, Z., Peng, Y., Li, B., Wu, Z. and Wang, Y.: Negative Aerosol-Cloud
1058   re Relationship From Aircraft Observations Over Hebei, China, Earth Sp. Sci.,
1059   doi:10.1002/2017EA000346, 2018.

1060   Zhao, C., Zhao, L. and Dong, X.: A case study of stratus cloud properties using in situ aircraft
1061   observations over Huanghua, China, Atmosphere (Basel)., doi:10.3390/atmos10010019, 2019.

1062   Zawadowicz, M. A., Suski, K., Liu, J., Pekour, M., Fast, J., Mei, F., Sedlacek, A., Springston, S., Wang,
1063   Y., Zaveri, R. A., Wood, R., Wang, J., and Shilling, J. E.: Aircraft measurements of aerosol and
1064   trace gas chemistry in the Eastern North Atlantic, Atmos. Chem. Phys. Discuss. [preprint],
1065   https://doi.org/10.5194/acp-2020-887, in review, 2020.

1066   Zheng, G., Wang, Y., Aiken, A. C., Gallo, F., Jensen, M. P., Kollias, P., Kuang, C., Luke, E., Springston,
1067   S., Uin, J., Wood, R., and Wang, J.: Marine boundary layer aerosol in the eastern North Atlantic:

1068   seasonal variations and key controlling processes, Atmos. Chem. Phys., 18, 17615–17635,

1069   https://doi.org/10.5194/acp-18-17615-2018, 2018.

1070 Zheng, G., Kuang, C., Uin, J., Watson, T., and Wang, J.: Large contribution of organics to condensational

1071   growth and formation of cloud condensation nuclei (CCN) in the remote marine boundary layer,

1072   Atmos. Chem. Phys., 20, 12515–12525, https://doi.org/10.5194/acp-20-12515-2020, 2020.

1073 Zheng, X., Xi, B., Dong, X., Logan, T., Wang, Y. and Wu, P.: Investigation of aerosol-cloud interactions

1074   under different absorptive aerosol regimes using Atmospheric Radiation Measurement (ARM)

1075   southern Great Plains (SGP) ground-based measurements, Atmos. Chem. Phys., doi:10.5194/acp-

1076   20-3483-2020, 2020.

1077 Zheng, Y., Rosenfeld, D. and Li, Z.: Quantifying cloud base updraft speeds of marine stratocumulus

1078   from cloud top radiative cooling, Geophys. Res. Lett., doi:10.1002/2016GL071185, 2016.

1079 Zheng, Y., Rosenfeld, D. and Li, Z.: A More General Paradigm for Understanding the Decoupling of

1080   Stratocumulus-Topped Boundary Layers: The Importance of Horizontal Temperature Advection,

1081   Geophys. Res. Lett., doi:10.1029/2020GL087697, 2020.

1082 Zhu, P. and Zuidema, P.: On the use of PDF schemes to parameterize sub-grid clouds, Geophys. Res.

1083   Lett., doi:10.1029/2008GL036817, 2009.

1084
1085

Table 1. Dates and time periods of selected non-precipitating MBL cloud periods

Case No.	Start Date	Start UTC	End Date	End UTC	Valid Samples
1	20160915	2200	20160916	0020	24
2	20170219	2110	20170220	0520	87
3	20170222	0830	20170222	1200	38
4	20170605	1430	20170605	1900	54
5	20170616	1230	20170616	1510	32
6	20170617	0320	20170617	0520	24
7	20170627	0020	20170627	0250	28
8	20170630	0530	20170630	0930	42
9	20170630	1400	20170630	1700	34
10	20170706	0140	20170706	0900	62
11	20170707	0130	20170707	1000	91
12	20170910	2100	20170911	0600	94
13	20170911	1930	20170911	2150	24
14	20170912	0820	20170912	1100	32
15	20171006	2110	20171006	2320	26
16	20180130	1030	20180131	0500	152
17	20180203	1930	20180204	0500	72
18	20180324	0210	20180324	0600	46
19	20180508	0730	20180508	1110	42
20	20180513	2130	20180514	1200	139

Table 2. Occurrence frequencies of large in-cloud r_e * under relatively high PWV conditions

PWV (cm)	1.2-1.4	1.4-1.6	1.6-1.8	2.8-2.0	2.0-2.2	2.2-2.4
$r_e > 12$ µm (%)	25.0	30.6	54.1	74.2	93.8	97.5
$r_e > 14$ µm (%)	1.25	1.77	7.4	17.7	31.9	20.1

*The occurrence of large r_e is defined when the r_e is found to be larger than 12 µm or 14 µm using the retrieved in-cloud vertical profiles.

Table 3. ACI_r calculated with respect to N_{CCN} theoretically at different supersaturation levels, under all PWV_{BL} conditions

PWV_{BL} (cm)	0.4-0.6	0.6-0.8	0.8-1.0	1.0-1.2	1.2-1.4	1.4-1.6	1.6-1.8	1.8-2.0	2.0-2.2	2.2-2.4
ACI_r (N_{CCN}@0.2%SS)	0.020	0.057	0.002	-0.014	0.108	0.076	0.145	0.151	0.221	0.175
(N_{CCN}@0.5%SS)	0.023	0.057	0.0002	0.024	0.129	0.121	0.309	0.136	0.293	0.159
(N_{CCN}@1.2%SS)	0.023	0.045	0.002	0.072	0.125	0.123	0.323	0.175	0.347	0.186

Table 4. The first three principal components from eigenanalysis

Eigenanalysis	PC1	PC2	PC3
Eigenvalues	2.17	1.10	0.91
Proportion of variance explained (%)	43.72	22.01	18.26
Cumulative proportion (%)	43.72	65.73	83.99
Correlations (Variables vs. PCs)	PC1	PC2	PC3
PWV_{BL}	-0.84	0.20	-0.11
D_i	-0.73	-0.48	-0.20
TKE_W	0.69	0.35	-0.44
$W_{dir,ns}$	0.52	0.60	-0.50
LTS	-0.43	0.58	0.65
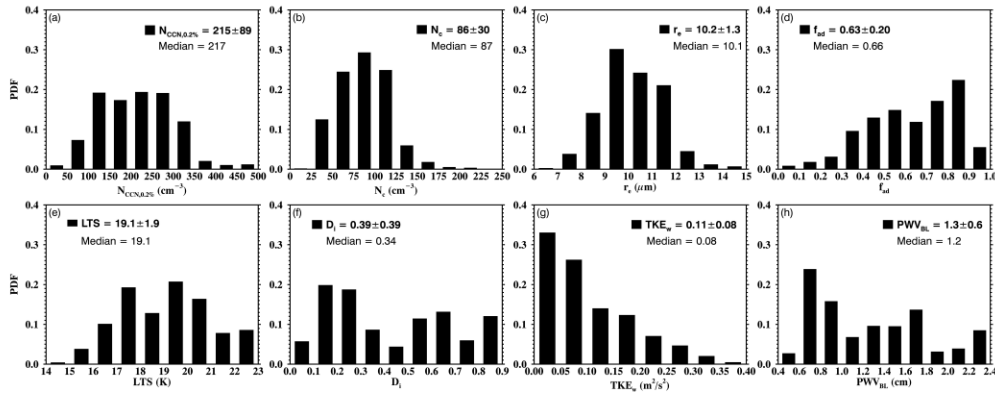
Figure 1. Probability distribution functions (PDFs), mean, standard deviation and median values of aerosol, cloud, and meteorological properties for 20 selected non-precipitating cloud cases at the DOE ENA site during the period 2016-2018. (a) Cloud condensation nuclei (CCN) number concentration at 0.2% supersaturation ($N_{CCN,0.2\%}$); (b) cloud-droplet number concentration (N_c); (c) cloud-droplet effective radius (r_e); (d) cloud adiabaticity (f_{ad}); (e) lower tropospheric stability (LTS); (f) decoupling index (D_i); (g) mean vertical component of turbulence kinetic energy (TKE_w); and (h) sub-cloud boundary-layer precipitable water vapor (PWV_{BL}).
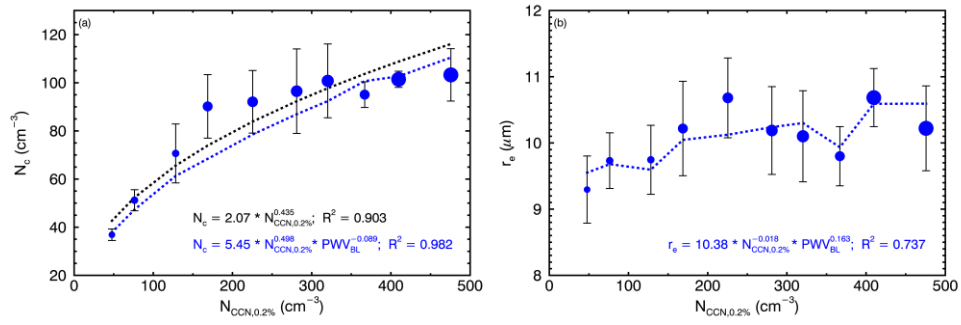
Figure 2. (a) N_c and (b) r_e as a function of $N_{CCN,0.2\%}$ (x-axis) and PWV (blue filled circles) for all selected samples. The larger blue circles represent relatively higher PWV values. Whiskers denote one standard deviation for each bin.
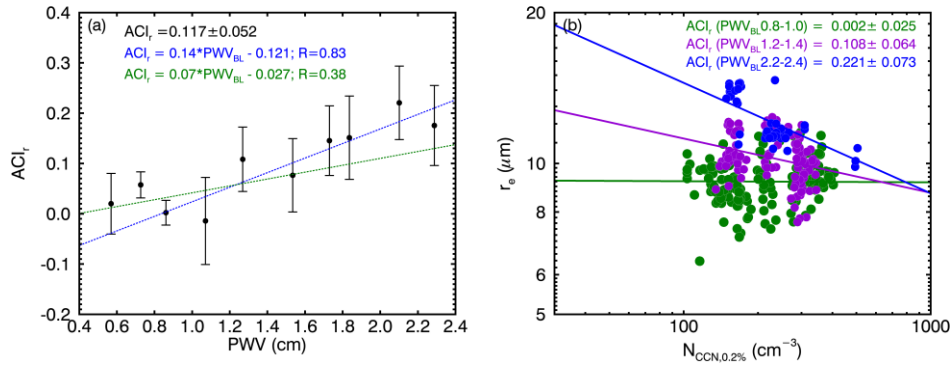
Figure 3. (a) Relationship of ACI_r (dots) to binned PWV_{BL}. Whiskers denote one standard deviation for each bin. Linear regressions are performed in relatively low PWV_{BL} regime (< 1.4 cm, green) and high PWV_{BL} regime (> 1.4 cm); and (b) illustration of ACI_r derived from r_e to $N_{CCN,0.2\%}$ in following three PWV_{BL} bins: 0.8-1.0 cm (green), 1.2-1.4 cm (purple), 2.2-2.4 cm (blue). The ACI_r represents the relative change of r_e with respect to the relative change of $N_{CCN,0.2\%}$, where positive ACI_r denotes the decrease of r_e with increased $N_{CCN,0.2\%}$ under binned PWV.
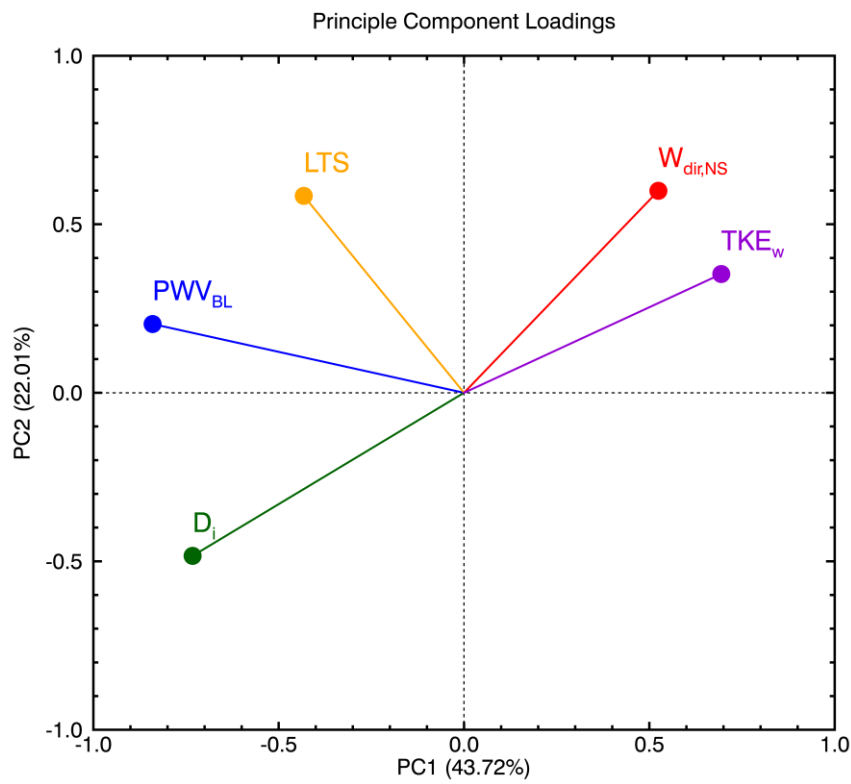
Figure 4. The projections of TKE_w (purple), $W_{dir,NS}$ (red), LTS (orange), PWV_{BL} (blue) and D_i (green) onto the first principal component (PC1) and the second principal component (PC2). The x-coordinates denote variables' correlations with PC1, and the y-coordinates denote variables' correlations with PC2.
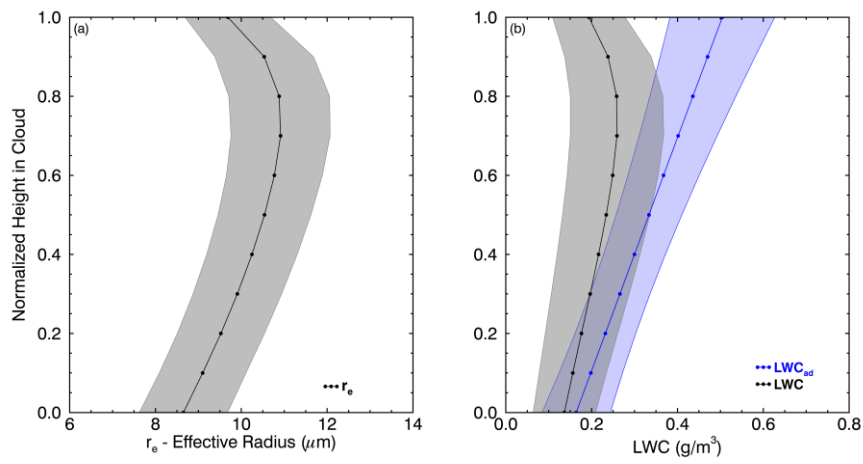
Figure 5. Normalized in-cloud vertical profiles of retrieved (a) r_e and (b) LWC (black) and calculated adiabatic LWC_{ad} (blue) for all selected cloud cases, 0 is cloud base and 1 is cloud top. Solid dotted lines denote mean values and shaded areas denote one standard deviation at each height.
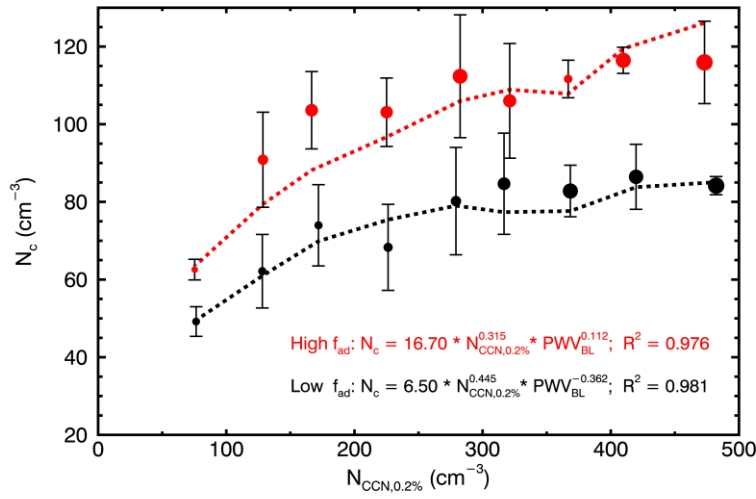
Figure 6. N_c as a function of $N_{CCN,0.2\%}$ (x-axis) and PWV (dots) for high adiabaticity f_{ad} (red) and low f_{ad} (black) regimes. The larger circles represent relatively higher PWV values. Whiskers denote one standard deviation for each bin.
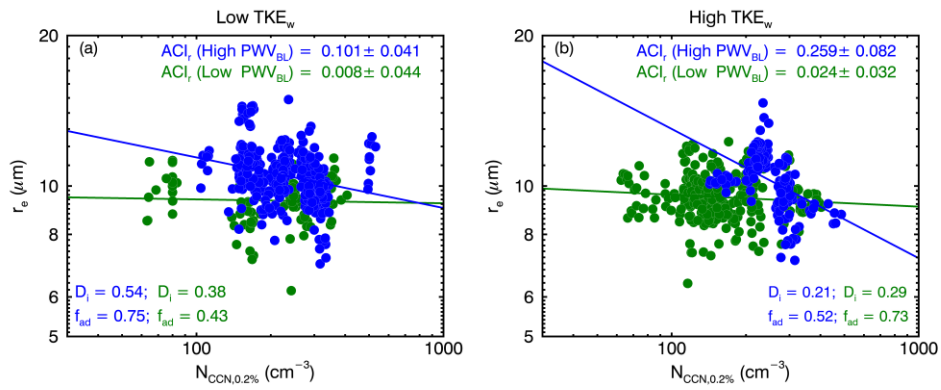
Figure 7. ACI_r derived from r_e to $N_{CCN,0.2\%}$ for (a) low TKE_w and (b) high TKE_w regimes. Samples in the low PWV regime are plotted in green, and samples in the high PWV regime are plotted in blue. The mean values of D_i and f_{ad} are displayed for each quadrant with the corresponding color-coded.
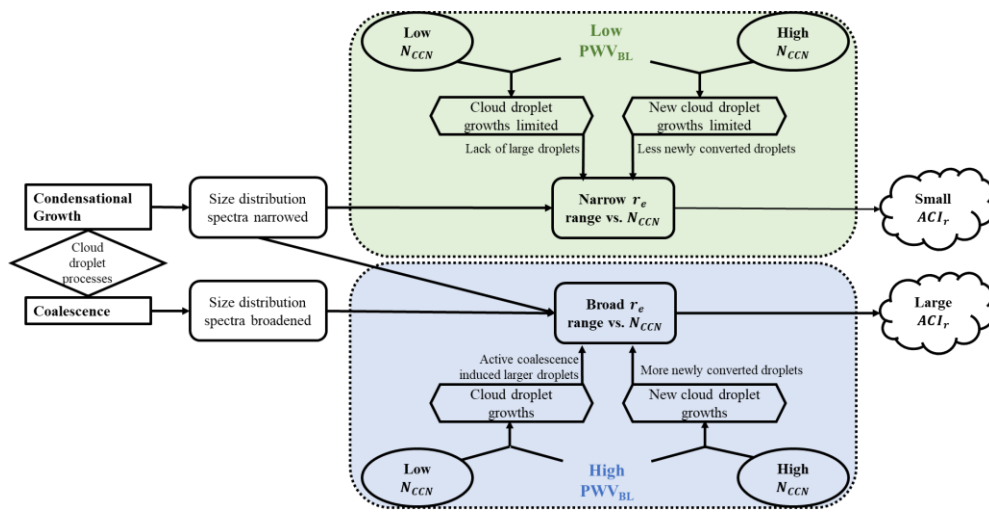
Figure 8. Theoretical mechanism of the responses of cloud droplet size distributions to different CCN intrusion, under relative insufficient (low PWV$_{BL}$) versus sufficient (high PWV$_{BL}$) water vapor availabilities.